

KERNFORSCHUNGSZENTRUM KARLSRUHE

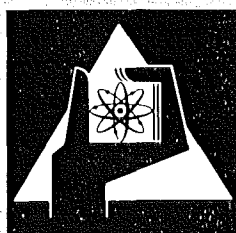
Januar 1975

KFK 2095
EUR 5200e

Institut für Angewandte Systemtechnik und Reaktorphysik
Institut für Neutronenphysik und Reaktortechnik
Projekt Schneller Brüter

Analysis of SEFOR Experiments

H.G. Bogensberger, L. Caldarola, F. Mitzel
W.J. Oosterkamp, D. Wintzer



**GESELLSCHAFT
FÜR
KERNFORSCHUNG M.B.H.**

KARLSRUHE

Als Manuskript vervielfältigt

Für diesen Bericht behalten wir uns alle Rechte vor

GESELLSCHAFT FÜR KERNFORSCHUNG M. B. H.
KARLSRUHE

KERNFORSCHUNGSZENTRUM KARLSRUHE

1974

KFK 2095
EUR 5200e

Institut für Angewandte Systemtechnik und Reaktorphysik
Institut für Neutronenphysik und Reaktortechnik
Projekt Schneller Brüter

Analysis of SEFOR experiments

H.G. Bogensberger, L. Caldarola⁺⁾ , F. Mitzel,
W.J. Oosterkamp, D. Wintzer

⁺⁾ EURATOM Karlsruhe

Gesellschaft für Kernforschung mbH., Karlsruhe

Analysis of SEFOR experiments

Abstract

The report describes methods and results of the analysis of several SEFOR zero power and power experiments.

With few exceptions, the analysis of zero power experiments confirms experiences which had been obtained by more simple zero power assemblies for the more recent GfK cross section sets and calculational methods.

The Doppler temperature coefficients as evaluated from several SEFOR Doppler experiments are in good agreement with GE results, although evaluation methods differ in several details.

The evaluated Doppler temperature coefficients are slightly overestimated by nuclear calculations. However, the overestimation is within the estimated uncertainties of the evaluations from experiments.

6.12.1974

Analyse von SEFOR Experimenten

Zusammenfassung

Der Bericht beschreibt Methoden und Ergebnisse der Analyse verschiedener Nullenergie- und Leistungsexperimente in SEFOR.

Die Analyse der Nullenergieexperimente bestätigt mit wenigen Ausnahmen die Erfahrungen, die für die neueren Querschnittsätze und Rechenmethoden der GfK an einfacheren Nullenergieanordnungen gemacht wurden.

Die aus verschiedenen Dopplerexperimenten in SEFOR ermittelten Doppler-Temperaturkoeffizienten sind in guter Übereinstimmung mit GE-Resultaten, obwohl sich die Auswertemethoden in verschiedenen Einzelheiten unterscheiden.

Ergebnisse nuklearer Berechnungen der Dopplerkonstanten liegen etwas höher als die aus den Experimenten abgeleiteten Werte. Die Überschätzung liegt jedoch innerhalb der Analyseunsicherheiten.

Table of Contents

	Page
1. Preface	1
2. Analysis of Zero Power Experiments	4
2.1 Summary	4
2.2 Criticality	6
2.3 Analysis of Material Worth Measurements	15
2.4 Fission Rate Distributions and Fission Ratios	22
3. Analysis of the Static Tests	29
3.1 Summary	29
3.2 Outline of the Calculations	29
3.3 Heat Transfer Model	30
3.4 Doppler Determination	32
3.5 Error Analysis	36
4. Analysis of the Transient Tests	41
4.1 Summary	41
4.2 Description of the Tests	42
4.3 Outline of the Analysis	42
4.4 Inverse Kinetics	45
4.5 Feedback Effects	46
4.6 Determination of the Average Decay Constant of the Delayed Neutrons	48
4.7 Determination of the Reduced Neutron Lifetime $1/\beta$	58
4.8 Doppler Evaluation	60
4.9 Error Analysis and Discussion	62

	Page
5. Analysis of Oscillator Experiments	66
6. Nuclear Doppler Calculations	73
6.1 Summary	73
6.2 Studies Concerning the Temperature Dependence of Effective Cross Sections	73
6.3 Variation of Doppler Results with Geometrical Models	77
6.4 Comparison of Results for Different Cross Section Sets	78
6.5 Errors Introduced by the Perturbation Theory Approximation	79
6.6 Additional Corrections	80
6.7 Comparison of Calculated with Experimental Results	81
7. Summary and Conclusions	84
Appendix A Geometrical Models and Material Densities for Neutrons Physics Calculations	86
Appendix B Supplementary Studies for B_4C Rods in SEFOR 1-D	101

1. Preface

This report describes the main procedures and results of GfK analysis of SEFOR experiments.

It is not the purpose of this report to describe in detail experimental conditions, data collection and processing, etc., which are well documented in several GE reports, for instance in /1/ through /5/.

Emphasis of our analysis work was put on those experiments, which were specifically planned for, and the experimental conditions of which were suited for evaluation of Doppler reactivity effects. The demonstration of the shut down capability of the Doppler reactivity effects during transient power situations caused by reactivity ramps and the demonstration of an expectable degree of agreement with quantitative theoretical results were the main, and achieved, goals of the SEFOR program /6/.

The more one is interested in a quantitative transfer of Doppler reactivity effect experience from SEFOR to other fast breeders with similar neutron spectra, the more it is important to be consistent in the cross section sets used, in the models for the physical effects involved and in the calculational procedures. The difference between "measured" and calculated Doppler constants sensitively depends on several details of evaluation and calculation. To a certain degree, such details are specific for

specific groups of investigators or even countries because of specific availability of cross section sets and codes and because of certain traditions in theoretical approximations. Details of this report might therefore be useful for those hypothetical future users of quantitative physical SEFOR information, who have access to GfK cross section sets and codes.

Besides of Doppler effect information (sections 3,4,5 and 6) the report discusses SEFOR experiences concerning criticality, material reactivity worth, fission rate distributions (section 2), effective decay constant of delayed neutrons, prompt neutron generation time (section 4) and fuel time constants for changes of the temperature profile (section 5).

References for Section 1

- /1/ G. Billuris et al.
SEFOR Plant Design
Fast Reactors National Topical Meeting, San Francisco,
April 1967, ANS-101
- /2/ L.D. Noble, C.D. Wilkinson
Final Specifications for the SEFOR Experimental Program
GEAP-5576, Jan. 1968
- /3/ Southwest Experimental Fast Oxide Reactor Development
Program
Quarterly Reports 10010
- /4/ L.D. Noble, F. Mitzel, B. Sarma, D. Wintzer, Y.S. Lu,
G. Kessler, G.R. Pflasterer, R.A. Becker, L. Mansur
Results of SEFOR Zero Power Experiments
GEAP-13588 (1970)
- /5/ L.D. Noble, A.M. Raberain, G.R. Pflasterer, F. Mitzel,
S. Derby, G. Kussmaul, R.A. Becker, B. Sarma, Y.S. Lu,
M. Plummer, Q. Baird, W.J. Oosterkamp
SEFOR Core 1 Test Results to 20 MW
GEAP-13702 (1971)
- /6/ L. Caldarola, D.D. Freeman, P. Greebler, G. Kussmaul,
F. Mitzel, L.D. Noble, G.R. Pflasterer, W.J. Ooster-
kamp, D. Wintzer
SEFOR Experimental Results and Application to LMFBR's
Proc. of the Int. Conf. on Engineering of Fast Reactors,
Karlsruhe, Oct. 9 - 13, 1972

2. Analysis of Zero Power Experiments

2.1 Summary

Methods and results of the analysis of some important criticality measurements, material reactivity worth measurements and fission rate distribution measurements are described in this section.

Calculated reactivity results are in reasonable agreement with experiments. Results obtained with the more recent GfK cross section sets are shown in the table below for 3 assemblies:

Cross section set	k_{eff} calc. ("experimental" is 1)		
	1 - C	1 - D	2 - A
MOXTOT 001	.991	.990	
KFKINR		.995	.998

The results are consistent with experience obtained for the two cross section sets by analysis of more simple Plutonium fuelled

configurations in zero power assemblies and indicate that there were no major errors in material distribution models and methodical procedures.

Fuel rod reactivity worths in assemblies 1-D and 2-A are overestimated by the calculations by amounts which plausibly can be explained by errors in the delayed neutron data and - in the case of assembly 1-D - by a slightly asymmetrical boron rod loading in the core. The overestimation of boron rod reactivity worths ($\sim 30\%$) in assembly 1-D indicates an overestimation of the moderating power of BeO in this assembly.

Fission rate distributions were underestimated near the axial and radial core boundaries by typically 20% when the calculations were normalized to experimental points near peak fission rate positions. Some of the reasons are identified, other possible reasons are discussed.

2.2 Criticality

Criticality calculations were done for three assemblies:

- Ass. 1-C (minimum critical core after replacing the very low Plutonium enrichment rods with normal fuel rods)
- Ass. 1-D (full size core with 14 B_4C rods)
- Ass. 2-A (full size core with 7 B_4C rods, BeO rods replaced with steel rods).

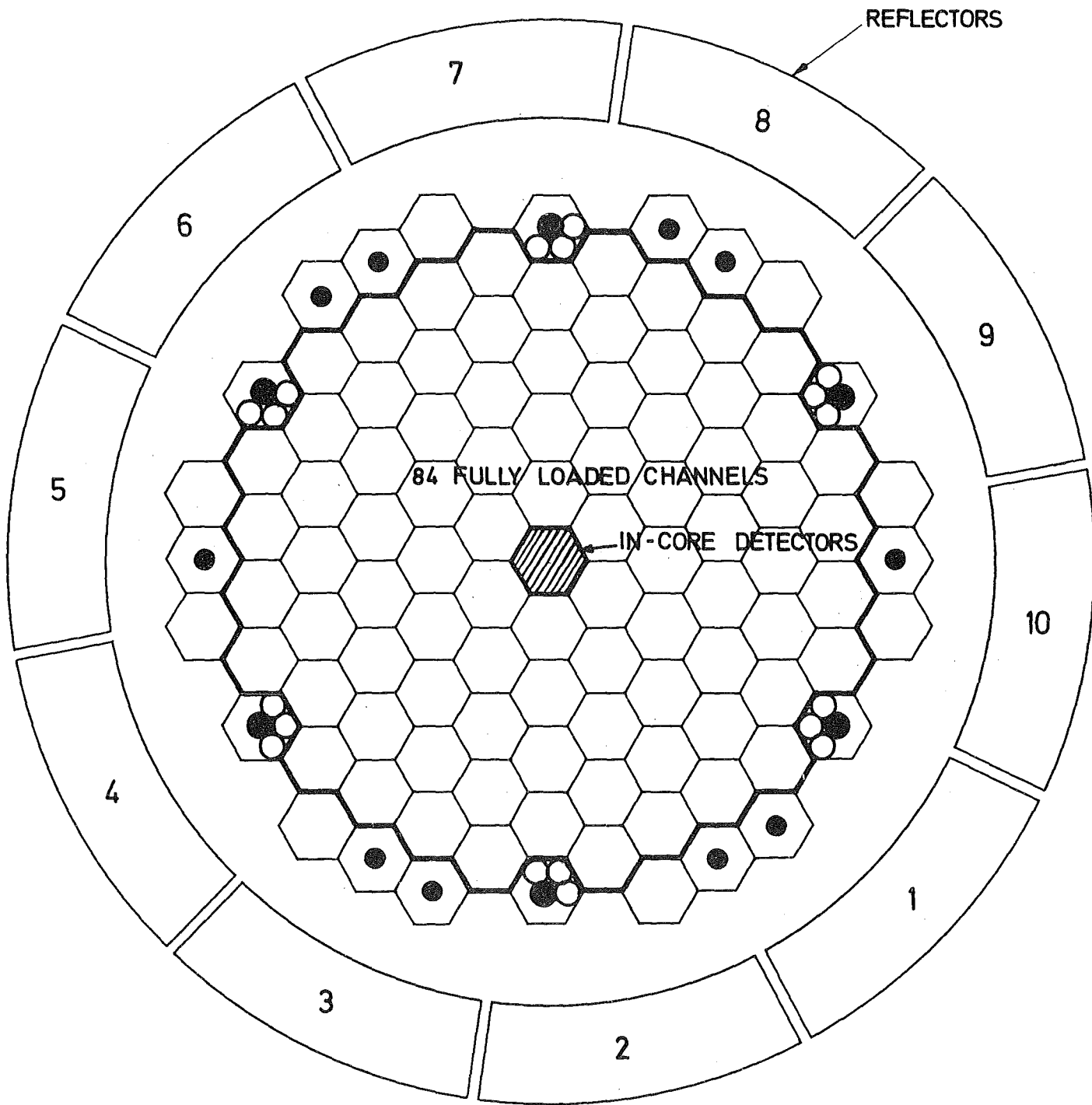
The loading patterns of these assemblies are shown in Figures 2.1 through 2.3. Appendix A contains the geometrical models and regional homogenized compositions that were used in the calculations.

Calculational Methods

Criticality calculations were based on two dimensional diffusion calculations with the code DIXY /1/. 26 neutron energy groups were used in all cases. The pronounced cell heterogeneity effects (the fuel rod diameter is 2.3 cm) were taken into account by using heterogeneity corrected cross sections which were computed by the cell code ZERA /2/. The fuel rod cell models used are shown in Figs. 5 and 6 of App. A: Corresponding material densities are listed in Table II of App. A. For purposes of comparison, some diffusion calculations were done for the homogenized core regions.

Comparative one dimensional (axial and radial) 26 group diffusion and S_8 -calculations were performed in order to evaluate reactivity corrections due to transport effects.

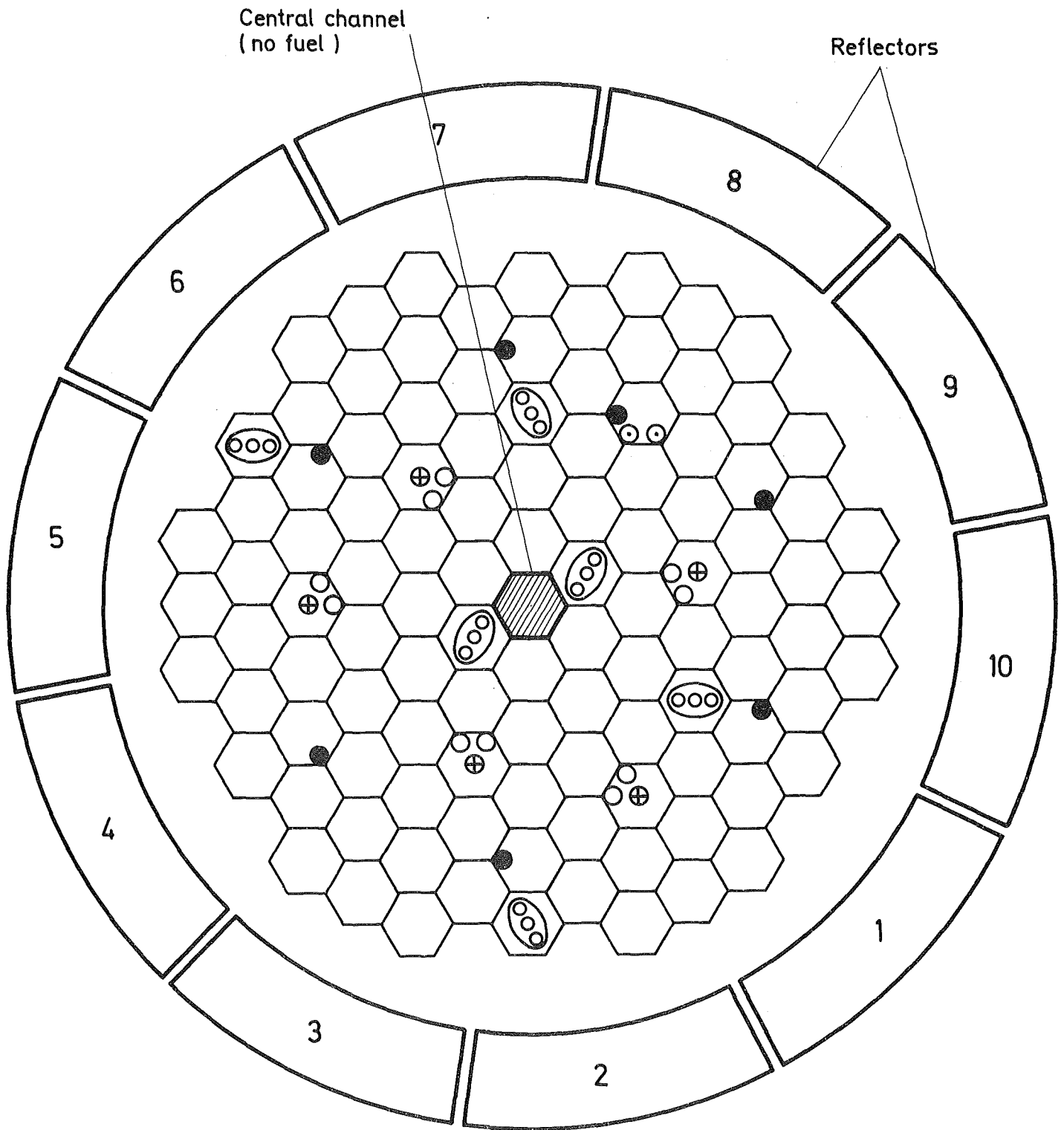
The reactivity calculations included the so called REMO correction /3/ which essentially is a correction of the elastic downscattering cross sections. It takes into account that the collision density spectrum in the specific reactor differs from the standard spectrum that was used to compute the microscopic cross sections of the 26 group set.



522 FUEL RODS
100 TIGHTENER RODS

● TIGHTENER RODS
○ FUEL RODS

FIG. 2.1 SEFOR MINIMUM CRITICAL LOADING (ASSEMBLY I-C)



- 617 Standard fuel rods
- 97 Standard stainless steel tightener rods
- 6 IFA BeO tightener rods
- 7 B₄C rods
- 2 GUINEA pig rods

- ⊙⊙⊙ IFA's
- B₄C rods
- Vacant fuel locations
- ⊕ Vacant tightener rod locations
- ⊙ GUINEA pig rods

Fig. 2.3 Core II Loading Assembly II - A

The SEFOR criticality measurements were done at a core temperature of 450° K. The atom densities listed in Appendix A correspond to this temperature. However, the diffusion and transport calculations were done with microscopic cross sections for 300° K, and a Doppler effect correction was necessary to extrapolate the results to 450° K.

The geometrical reactor models correspond to the situation that all reflector segments are in their upper position. During the measurements, criticality was achieved by partially lowering one or two control reflector segments. Thus, the calculations refer to a hypothetical more or less supercritical situation ($k_{\text{eff}} = 1 + \text{excess reactivity controlled by lowered reflectors}$). The excess reactivity was negligible only in Ass. 1-A and 1-C (minimum critical loadings).

Results of Criticality Calculations and Discussion

Most of calculations for Ass. 1-C and 1-D were performed with the MOXTOT cross section set. The main results are shown in Table I:

Table I:

Results of Criticality Calculations for Ass. 1-C and 1-D
Obtained with MOXTOT Cross Sections

Method or Correction	k_{eff}	
	1-C	1-D
2 dim. diffusion with heterogeneous cross sections	.9773	.9825
Transport correction	+.011	+.0104
REMO correction	+.004	+.004
Doppler correction 300°K→450°K	-.003	-.003
Excess tightener rods	+.0013	-
Reflector position	-	-.004
Total	.991	.990

The correction for excess tightener rods (BeO) was added because of the irregular BeO/fuel ratio at the core boundary in Ass. 1-C (compare Fig. 2.1). It was based on material worth measurements for BeO rods. The reflector position correction was based on control reflector reactivity calibration measurements.

The heterogeneity effects on reactivity were $\Delta k_{\text{eff}} = +.0069$ for Ass. 1-C and $\Delta k_{\text{eff}} = +.0110$ for Ass. 1-D.

The results indicate a consistent underestimation of about one percent of criticality in both assemblies. This is quite satisfying in view of cross section uncertainties and of methodical difficulties in dealing with the rather complicated geometry.

The underestimation of criticality is consistent with similar underestimations of zero power Plutonium assemblies reported by Kiefhaber /4/ for MOXTOT calculations.

For purposes of comparison, some one dimensional (radial) results of 26 group calculations for Ass. 1-C are shown in Table II for some other cross section sets.

Table II One Dimensional Reactivity Results for SEFOR 1-C and 1-D for Some Cross Section Sets

Set	1 - C		1 - D	
	k_{eff}	$k_{\text{eff}} - k_{\text{eff}}^{\text{(MOXTOT)}}$	k_{eff}	$k_{\text{eff}} - k_{\text{eff}}^{\text{(MOXTOT)}}$
MOXTOT 001	.9662	-	.9663	-
KFKINR	-	-	.9755	+.0092
NAPPMB 001	.9594	-.0068	.9592	-.0071
SNEAK 001	.9529	-.0133	-	-
KFKSET 040	.9873	+.0211	-	-

Criticality calculations for Ass. 2 A were performed with the KFKINR set and based on two dimensional homogeneous diffusion calculations. The results are shown in the table below:

	k_{eff}
2 dim. diffusion, hom. ^{a)}	.997
<hr/>	
Heterogeneity correction	+0.008
Transport correction ^{b)}	+0.010
REMO correction ^{c)}	-
Doppler correction 300 ^o K→450 ^o K	-0.002
Irregular core loadings ^{d)}	-0.008
Reflector position	-0.007
<hr/>	
Total	.998

Comments:

- a) For reasons of consistency with the heterogeneity correction and of comparison with Core 1 results, the number quoted is that for ZERA cross sections for lattice cell dimensions reduced by a factor 10^{-3} .
- b) The correction was assumed to be the same as for Ass. 1-D.
- c) The REMO correction was not calculated. The collision density spectrum of Ass. 2 A is similar to the spectrum used for the evaluation of KFKINR cross section set. Based on experience with REMO corrections for assemblies with similar spectra it is estimated that the REMO correction is smaller than .001.
- d) The main contribution is due to 10 vacant fuel rod locations. Additional contributions are for the presence of 5 vacant tightener rod locations and for the presence of 2 Guinca Pig rods (see Fig. 2.3). The corrections were based on material worth measurements.

An exact comparison with results for Ass. 1-D is not possible. However, Table II indicates a k_{eff} difference of .009 between KFKINR and MOXTOT calculations, neglecting corrections. Minor differences in the corrections for the two cross section sets can be expected from the REMO correction, which is .004 for MOXTOT assumed to be negligible for KFKINR. The estimate for the KFKINR result for Ass. 1-D is therefore:
 $.009 + .009 - .004 = .995$

The difference between this number and .998 for Ass. 2 A is not as small as the MOXTOT-difference between Ass. 1-C and 1-D, but it is within the expected uncertainties. Some possible reasons for the difference are:

- an overestimation of the B_4C rod worth in Ass. 1-D (see below)
- errors in the geometrical modelling of B_4C containing regions in the core
- errors in the moderating power of BeO and SS and in the neutron absorption of steel,
- differences between the (not calculated) KFKINR REMO correction for Ass. 1-D and 2-A
- differences in the impact of various possible cross sectional errors of the KFKINR set for the softer 1-D spectrum and the harder 2-A spectrum on k_{eff} .

Despite of the .3% inconsistency of the KFKINR results for Ass. 1-D and 2-A, both reactivity results are rather close to 1, which again is consistent with other satisfying experiences with criticality calculations for Plutonium fuelled critical assemblies with this cross section set.

In summary, the criticality calculations for the three SEFOR assemblies analyzed indicate, that there are no major errors in geometrical models and methodical procedures.

2.3 Analysis of Material Worth Measurements

Material reactivity worth experiments in SEFOR were performed by removal or exchange of rods of certain materials at various radial positions in the core. Experimental details are described in /5/ and /6/.

Our general calculational procedure for material reactivity worths was the application of perturbation theory to two dimensional 26 group neutron flux and adjoint distributions.

Fig. 2.4 and Fig. 2.5 show measured and calculated (with the KFKINR set) fuel rod reactivity worths as functions of the radial position in the core. The fuel rod worth is overestimated by about 10% for all positions in Core 1 (Ass. 1-D). The overestimation is essentially reduced for Core 2 (Ass. 2-A).

Boron rod reactivity worths in Core I are overestimated by typically 30% with the KFKINR set and by typically 10% in Core II (compare Figs. 2.6 and 2.7) Fig. 2.6 demonstrates that the situation in Core 1 is even worse for the MOXTOT set.

Comparative cell calculations for evaluation of flux depressions in and around B_4C rods in Core 1 led to a 6 percent decrease of the neutron capture rate in B_4C compared to the homogeneous case (compare Appendix B). A similar correction was not calculated for Core 2. However, from the difference of the neutron spectra in Ass. 1-D and Ass. 2-A, it can be estimated that the Core 2 correction would not be essentially smaller.

Cell calculations also showed that the heterogeneity correction for the fuel rod reactivity worth is less than 2%.

A possible contribution to the overestimation of reactivity worths in Ass. 1-D is the slightly asymmetrical boron rod loading in this assembly, resulting in a certain flux and adjoint tilting. Most of the rod worth measurements were done along a radius extending from the center towards

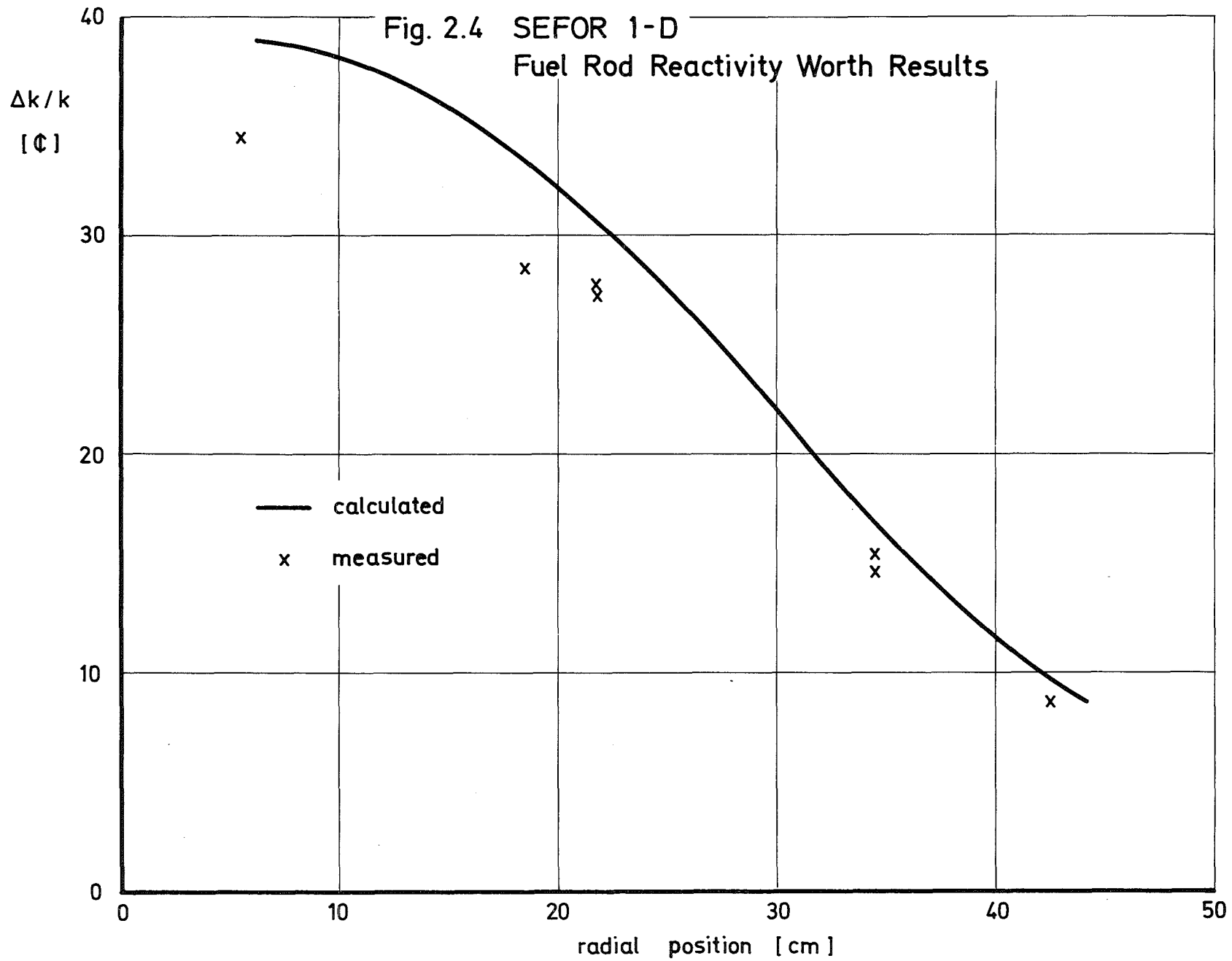
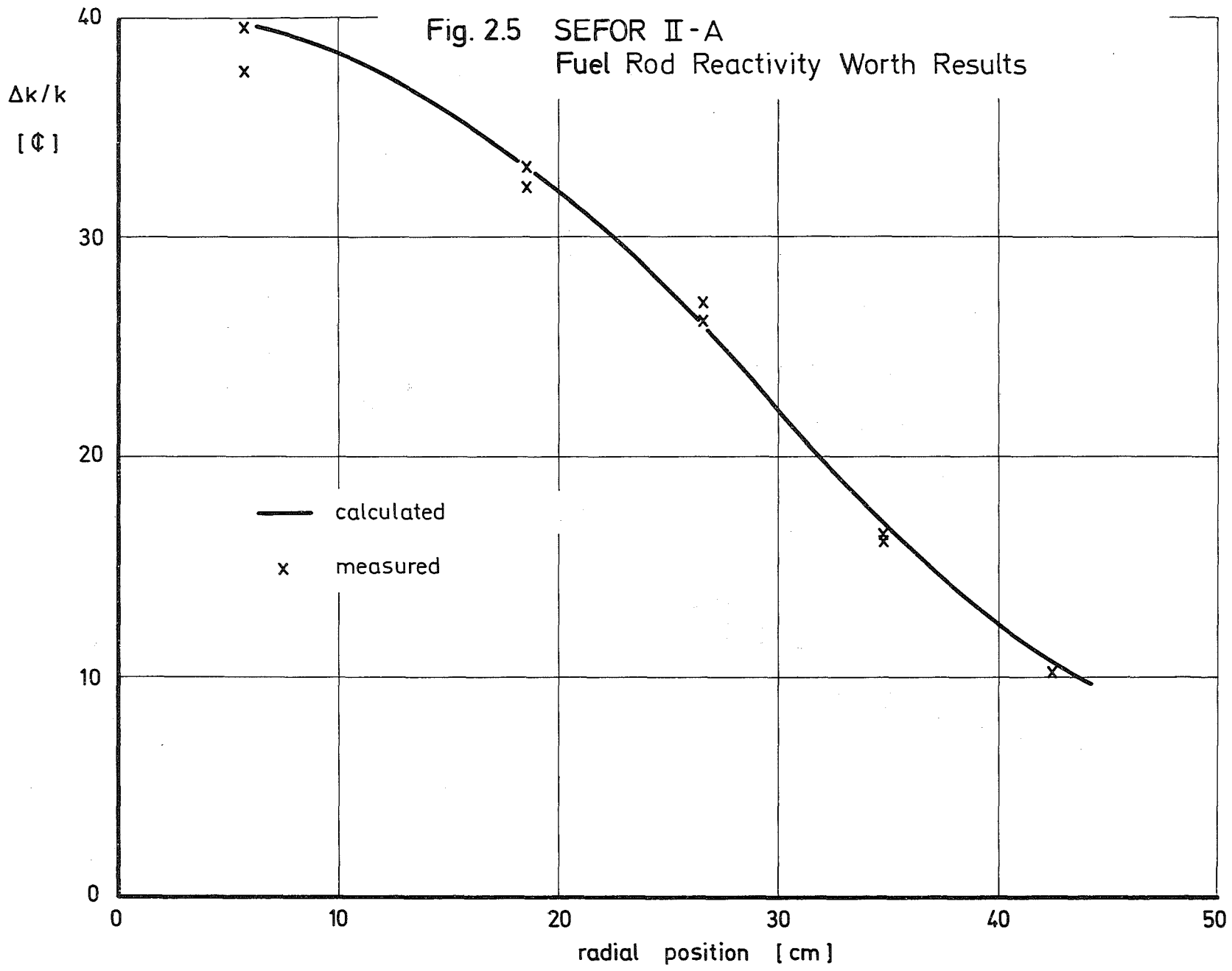


Fig. 2.5 SEFOR II-A
Fuel Rod Reactivity Worth Results



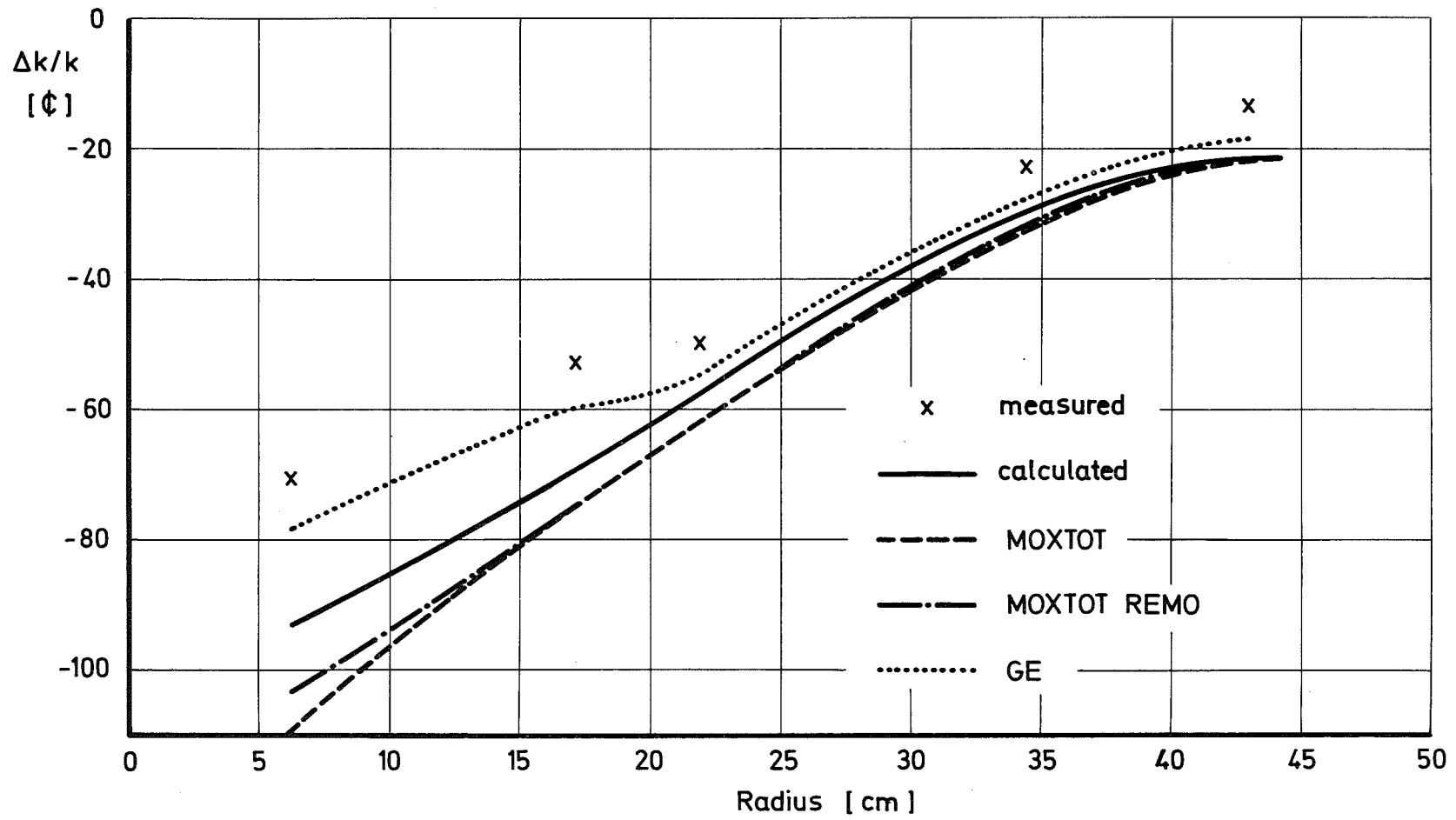
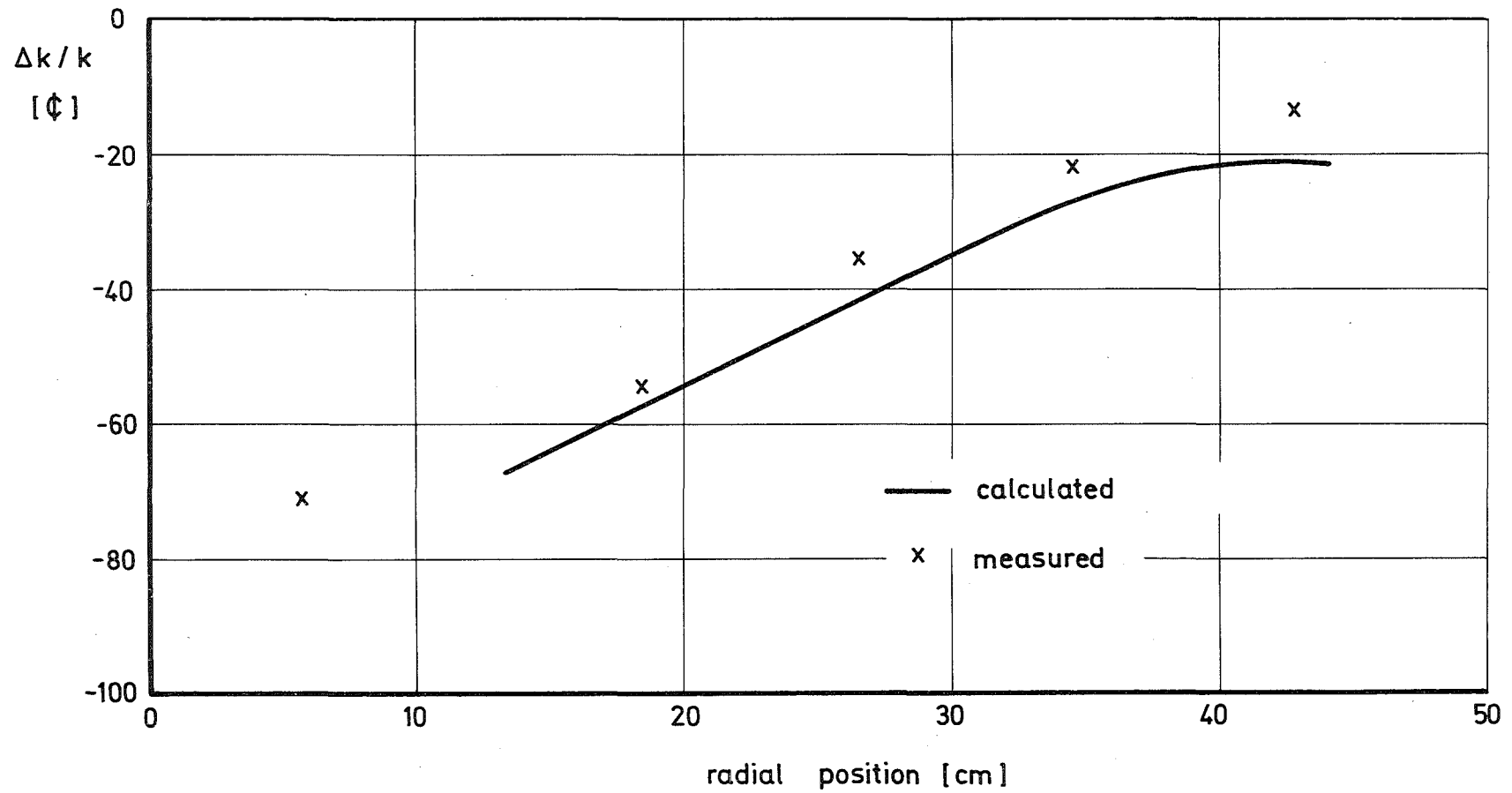


Fig. 2.6 SEFOR I-D
Boron Rod Reactivity Worth Results

Fig. 2.7 SEFOR 2-A
Boron Rod Reactivity Worth Results



the gap between reflectors 1 and 10 (compare Fig. 2.2). If one draws a core diameter in Fig. 2.2 perpendicular to this direction, one recognizes that more boron is on the right half of the core, where most of the measurements were done. One would then expect somewhat higher reactivity worths at the opposite side of the core (towards the intersection between reflectors 5 and 6). The only points in Fig. 2.4 and Fig. 2.6 measured at this side are those at a radial position of 21.8 cm. In fact, the ratio between calculation and experiments is lower by 5 to 10 per cent at this position.

Two dimensional (r,z) diffusion theory calculations described in App. B show that this order of magnitude can be expected as flux tilting effect on rod worths caused by the asymmetrical boron loading. Similar effects in Ass. 2-A are expected to be very small (compare the boron loading pattern, Fig. 2.3).

All reactivity worth calculations expressed in β are subject of possible systematical errors introduced by errors in β_{eff} , the fraction of delayed neutrons. More recent differential and integral measurements of this fraction at Los Alamos /7/, /8/ and in SNEAK indicate values for β_{eff} in U-Pu fuelled assemblies which are higher by about 5 to 10 per cent than those calculated (as usually) with Keepins /9/ data. This would reduce the overestimation of material reactivity worths in the SEFOR assemblies by about the same amount.

Additional reasons for the difference between calculated and measured B_4C reactivity worths must exist for Ass. 1-D. One suspects an overestimation of the moderating power of the BeO rods in this assembly, which would lead to an overestimation of the low energy part of the neutron spectrum. One should expect a similar overestimation by the calculations of the ratio $1/\beta_{eff}$ (1 is the prompt neutron generation

time), because $1/\beta_{\text{eff}}$ is proportional to the reactivity worth of a $1/v$ -absorber distributed throughout the reactor. In fact, this ratio was overestimated by 21% in Core I and by 8% in Core II (by two dimensional diffusion calculations with the KFKINR-set). The table below shows absolute numbers for $1/\beta_{\text{eff}}$.

Cross Section Set	Ass. 1-D	Ass. 2-A
MOXTOT	174.1 μs	--
KFKINR	168.7 μs	151 μs
EXPERIMENT ⁺⁾	140.5 μs	140 μs

⁺⁾ Noise measurements

2.4 Fission Rate Distributions and Fission Ratios

Fission rate distributions were measured in SEFOR by foil irradiation and subsequent fission product gamma activity measurements /5/, /6/. Results of these measurements are shown together with calculational results in Figs. 2.8 through 2.13. Calculated distributions are normalized to measurements near the core center. They are based on two dimensional 26 group diffusion calculations with the MOXTOT set.

The graphs show a rather consistent underestimation of the fission rate near the axial and radial core boundary. Similar underestimations were found by two dimensional 13 group diffusion calculations performed by GE. It can also be seen that the axial fission rate distributions are not accurately calculated in the expansion gap. Estimated experimental uncertainties are $\pm 5\%$ for the axial profiles and $\pm 10\%$ for the radial profiles /5/.

It has not been possible to explain completely the deviations shown. Radial transport calculations (S_8 - approximation) led to a 2.1% increase of the power density near the radial core boundary, but to negligible changes of the axial power distribution.

The complicated geometrical arrangement near the core boundary might well be one of the reasons for calculational inaccuracies. Comparative axial diffusion calculations led to an increase of the power density at the bottom and the top of the core of 3.8%, when a more detailed geometrical model was used to describe the material distribution at and beyond the core edges (the number of axial regions was increased in these calculations from 8 to 14). In the radial direc-

FIG. 2.8

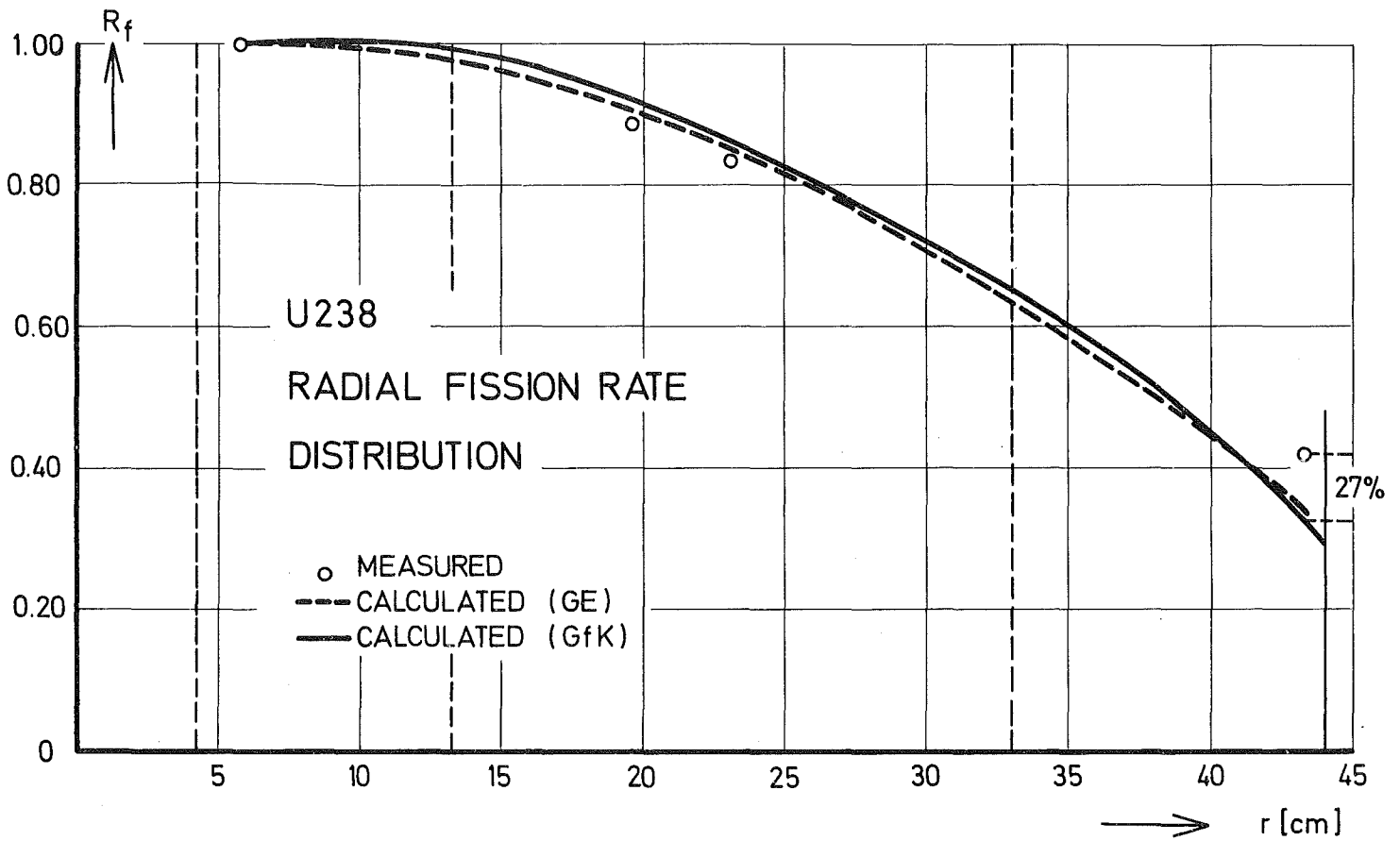


FIG. 2.9

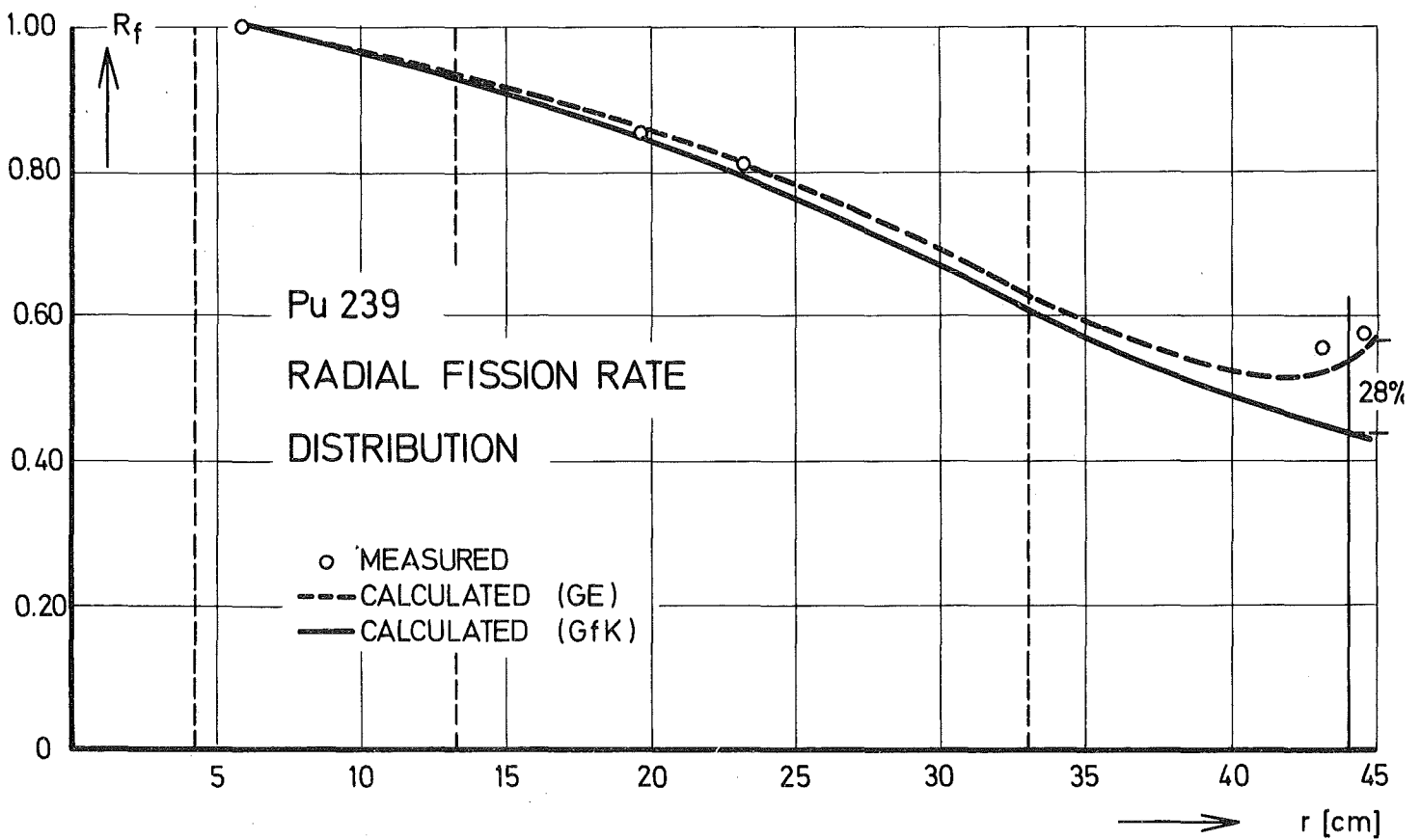


FIG. 2.10

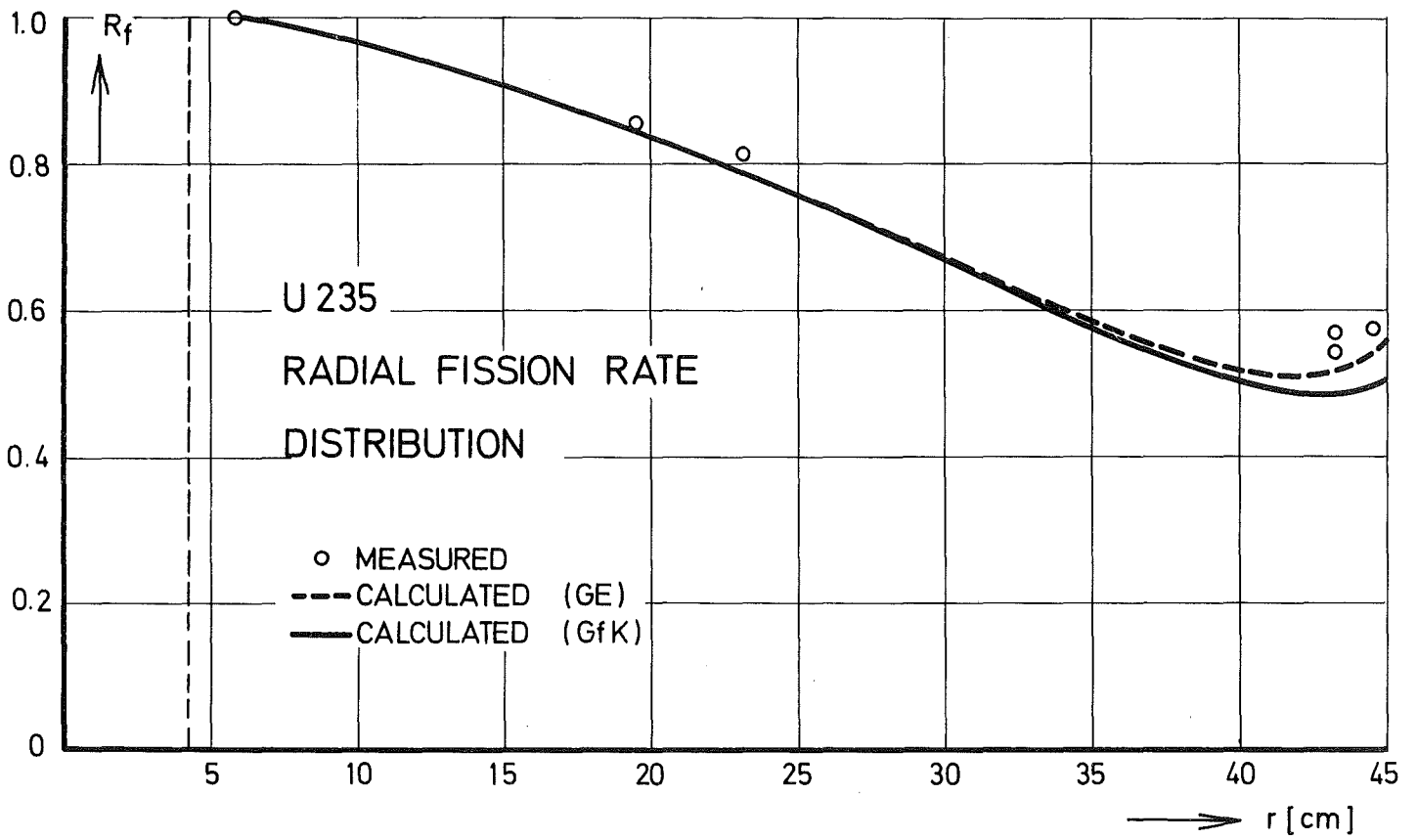


FIG. 2.11

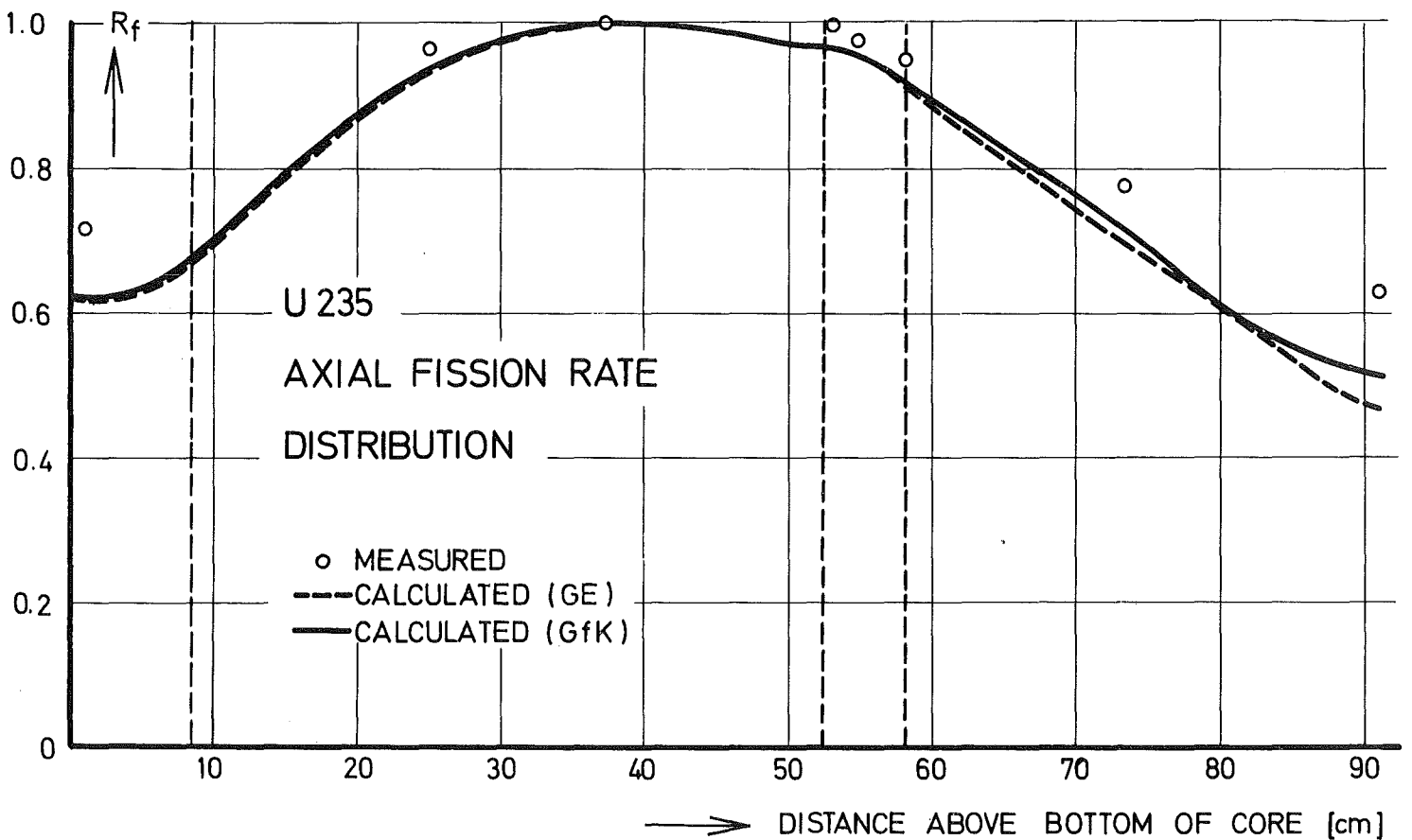


FIG. 2.12

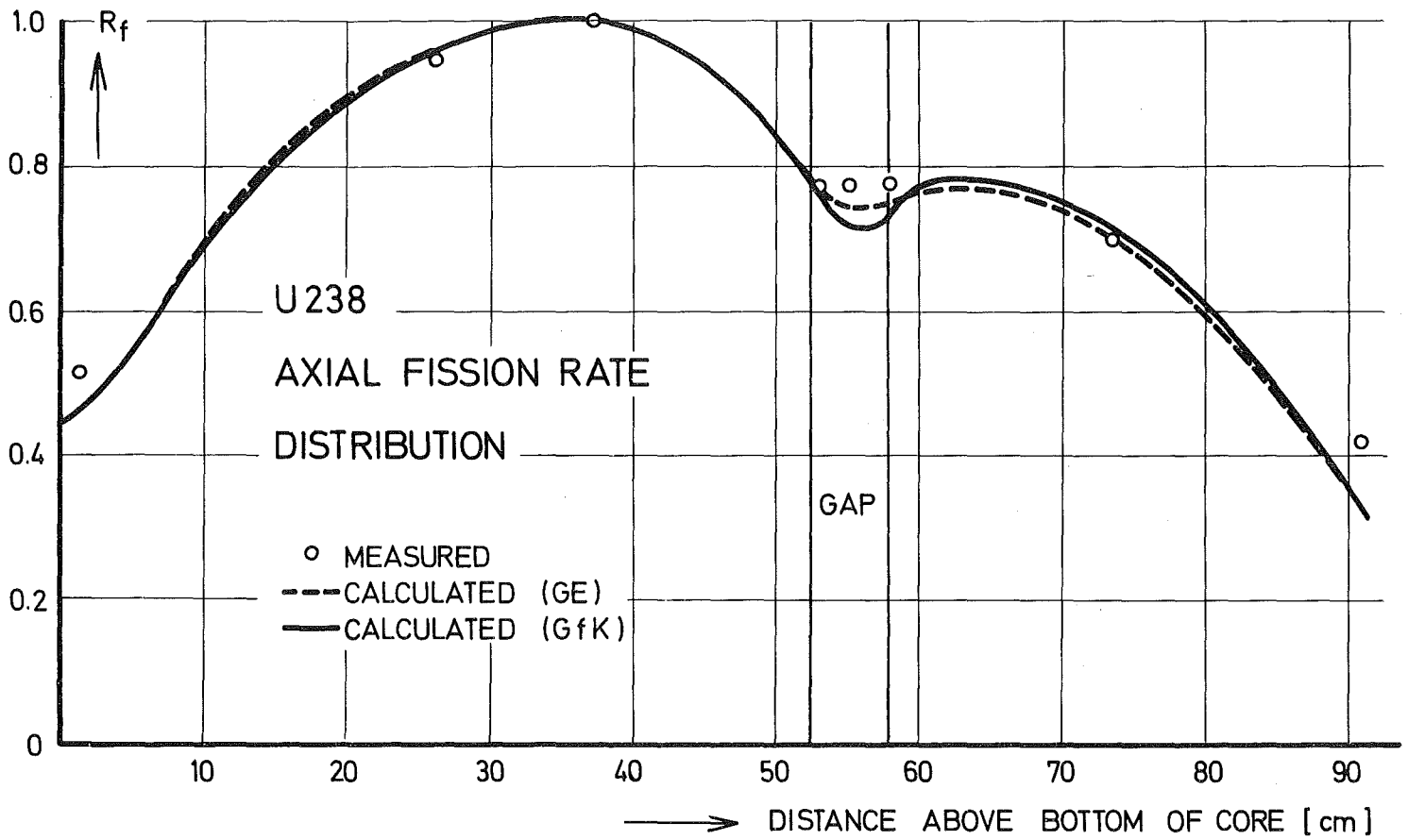
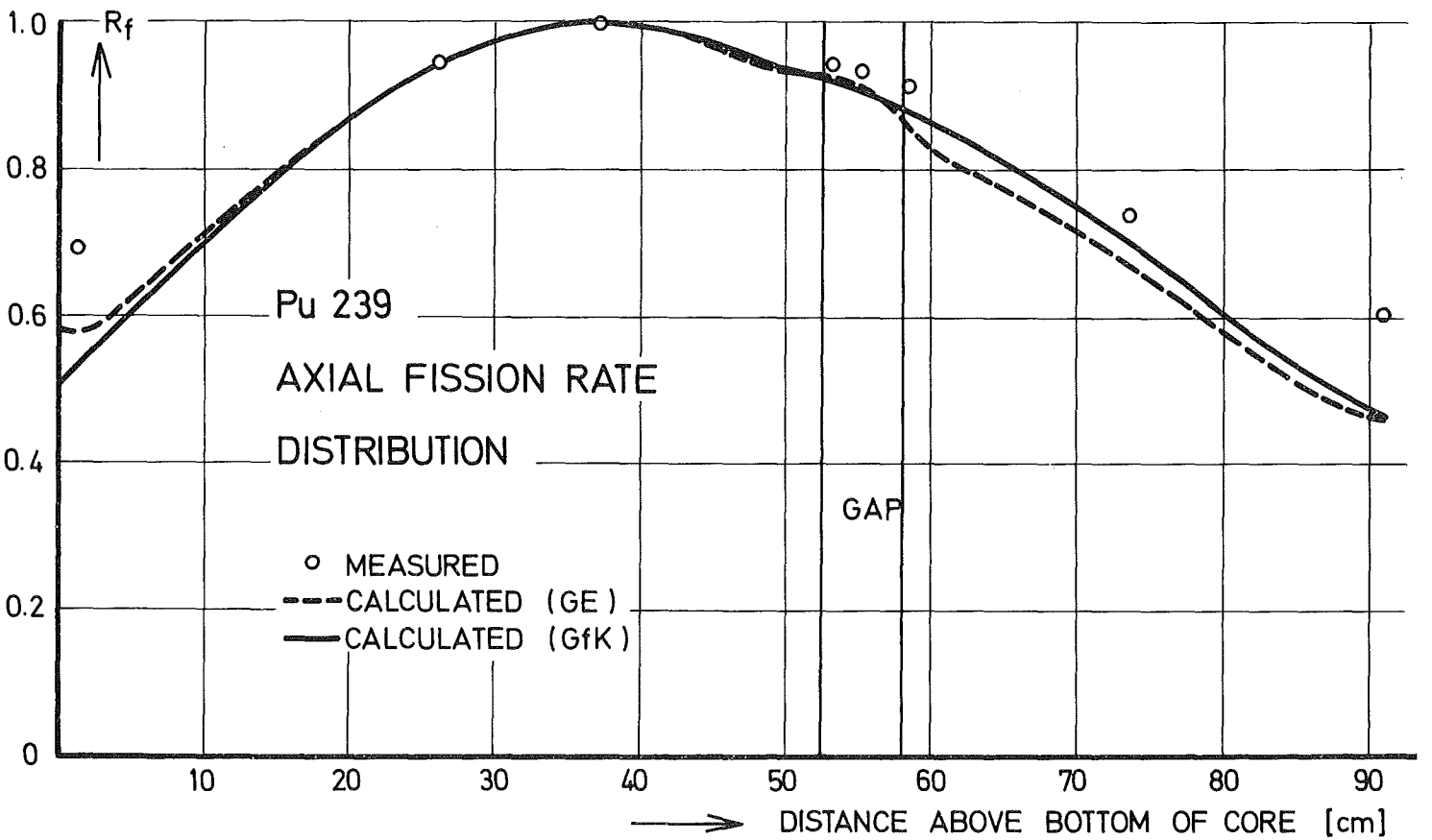


FIG. 2.13



tion, a sufficiently detailed description of the core edge region is not possible in cylindrical geometry (compare Fig. 2.2).

Expected methodical errors are also due to the treatment of resonance shielding effects near the core boundaries, where the shielding effects are certainly less than within the core. In the first instance, these effects would increase the resonance fissions in ^{239}Pu and ^{235}U near the core boundaries compared to our calculational results. ^{238}U fission rates would be increased indirectly by additional fast neutrons due to increased resonance fissions in ^{239}Pu .

The results of one dimensional radial diffusion calculations (Table III) give an impression about the dependence of power distribution parameters on cross section sets. P_r/\hat{P} is the ratio between power density at the radial core boundary and maximum power density.

Table III P_r/\hat{P} for Some Cross Section Sets

Set	P_r/\hat{P}
MOXTOT	.449
KFKINR	.446
NAPPMB	.457
SNEAKOO1	.447
KFKSETO40	.416

Similar (relative) differences were found for axial power distribution calculations.

An other suspected reason for the fission rate distribution discrepancies is an underestimation of neutrons returning from the nickel reflectors because of errors in the Ni cross sections used.

Approximate fission ratios at peak power position as obtained from the 1.6 MeV ^{140}La gamma decay peak of the irradiated foils /5/ are listed in Table IV together with calculated (MOXTOT) results. The estimated experimental uncertainty (2σ) is $\pm 10\%$.

Table IV Measured and Calculated Fission Ratios

Ratio	Experiment	Calculation 2-dim.	Calculation 0-dim. +)
σ_{f8}/σ_{f5}	.0252	.0236	.0252
σ_{f9}/σ_{f5}	.905	.857	.866
σ_{f8}/σ_{f9}	.0278	.0275	.0290

+) from cell calculations with energy independent critical buckling

Convincing conclusions upon errors in the calculated neutron spectrum can not be drawn from these numbers. The difference between experimental and two dimensional results is consistent with experience obtained with the MOXTOT set by analysis of SNEAK and ZPR-III Pu assemblies.

References for Section 2

- /1/ H. Küsters: Progress in Fast Reactor Physics in the Federal Republic of Germany - KFK-1692 (1973)

- /2/ D. Wintzer: Zur Berechnung von Heterogenitätseffekten in periodischen Zellstrukturen thermischer und schneller Kernreaktoren - KFK-743

- /3/ H. Küsters et al.: The Group Cross Section Set KFK-SNEAK; Preparation and Results - KFK-608 (1967)

- /4/ E. Kiefhaber: The KFKINR-Set of Group Constants; Nuclear Data Basis and First Results of its Application KFK-1572 (1972)

- /5/ L.D. Noble et. al.: Results of SEFOR ZORO Power Experiments GEAP-13838

- /6/ L.D. Noble, G. Kussmaul, S.L. Derby: Experimental Program Results in SEFOR Core II - GEAP-13838

- /7/ C.F. Masters, M.M. Thorpe, D.B. Smith: Nucl. Sci. Eng. 36, 202 (1969)

- /8/ M.S. Crick, A.E. Evans: Nucl. Sci. Eng. 47, 311 (1972)

- /9/ G.R. Keepin: Physics of Nuclear Kinetics Addison-Wesley, Palo Alto, 1965

3. Analysis of the Static Tests

3.1 Summary

The Doppler coefficient has been determined by the use of the measured reactivity feedback at different power levels. For this purpose the temperatures at different points in the reactor have been calculated using a model that takes into account restructuring of the fuel.

A Doppler constant of $A_D = -2.3 \pm .3 \%$ for Core I, $A_D = -1.8 \pm .3 \%$ for Core II has been obtained.

Experimental details of the static Doppler measurements are described in /1/ and /2/.

3.2 Outline of the Calculations

The reactor was described for the temperature calculations by about 100 regions. For each of these regions the linear pin power in W/cm was calculated for a given thermal power of the reactor. Fuel temperature was then calculated going from the gap inward. The thickness of the gap between fuel and cladding was calculated from the expansion of both using the average temperatures. A few iterations were necessary as the temperature drop across the gap and thus the fuel average temperature is very sensitive to the thickness of the gap. In case that there was no gap a constant heat conductivity was used. The fuel temperatures are then calculated. Restructuring of the fuel was taken into account when the fuel temperatures

exceeded threshold values of 1650°C for 97% density and 2150°C for 99% density. The central hole was then calculated from the conservation of mass. For subsequent power ascension it has been assumed that the reactor had operated at 20 MWth and the interfaces between fuels at different densities remained at the position which they reached at 20 MWth. The contribution of each region to the Doppler effect was calculated using the fuel average temperature rise and a global flux times adjoint flux weighting function.

3.3 Heat Transfer Model

We assumed that the gap can be described by

$$\delta = a + \gamma_c r_c \cdot T_c - \gamma_f \cdot r_f \cdot T_f \quad (1)$$

where $a = .19$ mm is the initial gap at 0°C

$r_c = 11.3$ mm is the inner radius of the cladding at 0°C

$r_f = 11.11$ mm is the radius of the fuel pellets at 0°C

$T_c =$ is the calculated clad temperature

$T_f =$ is the average fuel temperature

$\gamma_c = 17.62 \times 10^{-6}/^\circ\text{C}$ is the thermal expansion coefficient for SS

$\gamma_f = 7.54 \times 10^{-6} (1. + 13.85 \times 10^{-4} T_f)$ is the thermal expansion coefficient for the fuel

For the temperature drop over the gap the heat conduction formula of Kaempf /3/ has been used

$$\Delta T = \frac{X}{2\pi r_f} \cdot \frac{\delta}{k^+} \cdot \left[1 - \frac{\delta}{k^+} \left(4 P_{st} \cdot T^3 + \frac{.79}{8} \cdot \frac{X}{T} \cdot \frac{1}{2\pi r_f} \right) \right] \quad (2)$$

where X = is the linear power rating of the pin in (W/mm)

$$k^+ = 1.58 \times 10^{-5} T^{.79}$$

$$P_{st} = .378 \times 10^{-13} W_{mm}^{-2} O_K^{-4}$$

T = is the temperature of the outer surface of the fuel (°K)

Eq. (2) has been used for gap widths δ greater than 0.05 mm. For $0 < \delta < .05$ mm a linear interpolation between Eq. (2) and a constant value for the heat resistivity of $1^\circ C \text{ cm}^2 \text{ w}^{-1}$ has been used.

In case that the gap was closed a value of the heat resistivity of $1^\circ C \text{ cm}^2 \text{ w}^{-1}$ was used.

For the fuel itself the recommended values of Schmidt /4/ for the heat conductivity were used

$$\Lambda = \frac{(1.144x(1.-2.5x(1.-x_\theta)))}{(10.8+5.4+.0235x\theta))x(1.-2.74x10^{-8}xT^2+2.5x10^{-14}xT^4)}$$

where $\theta = T$ for $T < 1950^\circ C$

$\theta = 1950$ for $T > 1950^\circ C$

x_g is the fraction of the theoretical density of the fuel and has the following value depending on the maximum local temperature reached in the history of the reactor

$$\begin{aligned}x_g &= .92 \text{ for } T_{\max} < 1650^{\circ}\text{C} \\x_g &= .97 \text{ for } 1650 < T_{\max} < 2150^{\circ}\text{C} \\x_g &= .99 \text{ for } T_{\max} > 2150^{\circ}\text{C}\end{aligned}$$

The calculated temperature rise agrees to within 10% with the temperature rise (Fig. 3.1) as measured in the Core II instrumented fuel assemblies during the ascension to power. (The Core I instrumented fuel assemblies had certain malfunctions, and their temperature data are less suited for a comparison with calculations than the Core II data.)

3.4 Doppler Determination

For each region of the reactor a constant linear power per MW reactor output has been assumed. It was further assumed that the power could be separated axially and radially. The power distribution is given in Fig. 3.2 and Fig. 3.3. A maximum rating of 65 W/mm was obtained (see Table I).

The boundaries of the columnar growth region and the central void were calculated for a reactor power of 20 MWth. Average fuel temperatures were then calculated with these boundaries for different

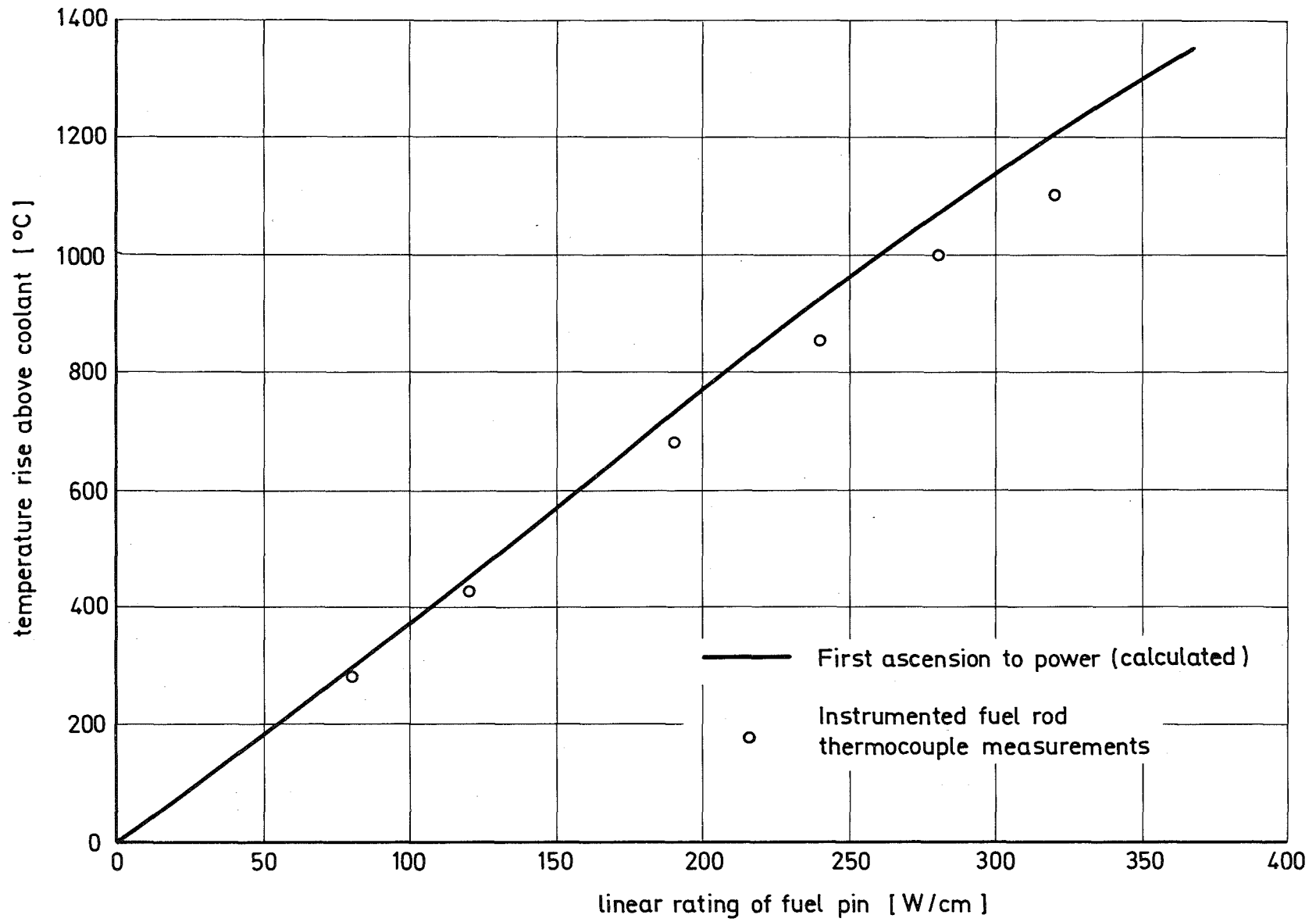


Fig.3.1 CORE II IFA Temperatures

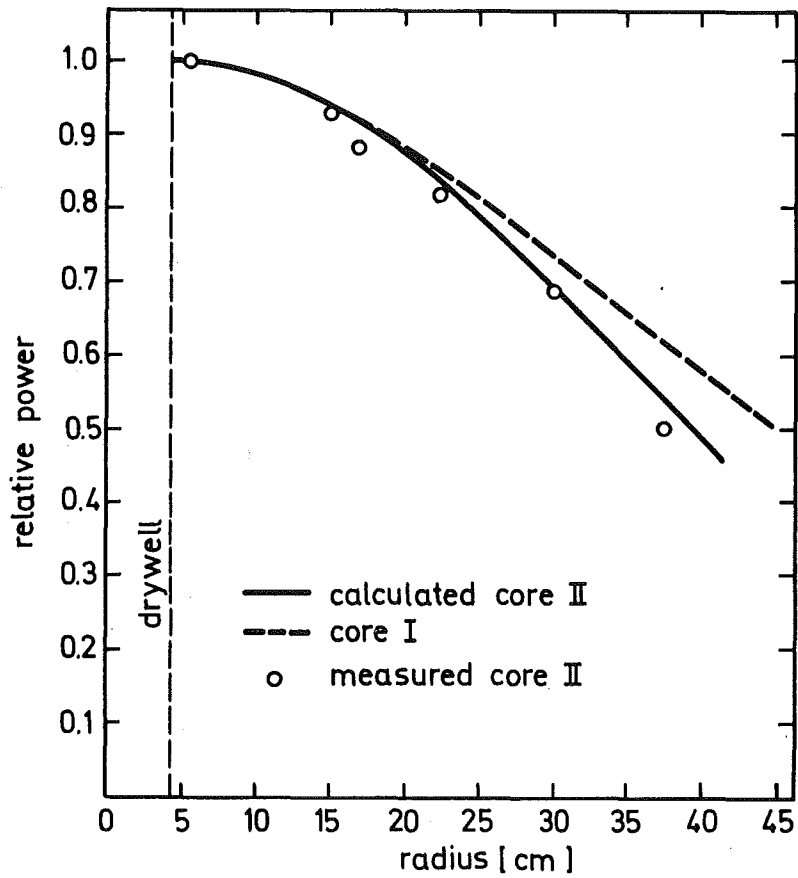


Fig. 3.2 Radial Power Distribution

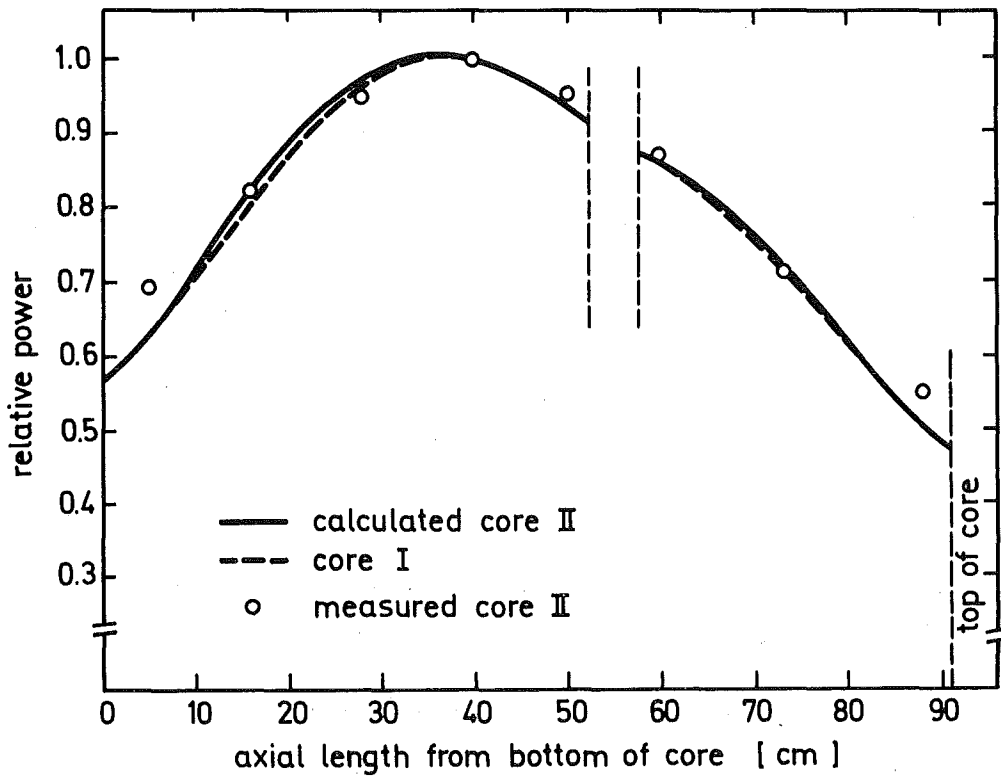


Fig. 3.3 Axial Power Distribution

Table I Fuel Data for Temperature
Calculations

Mass of the fuel	2150 kg
Density	10000 kg/m ³
Fraction of energy released in the fuel	.997
Average fuel rating at 20 MWth	9.1 KW/kg
Fuel pellet diameter	11.13 mm
Average linear rating	35.4 w/mm
Maximum to average power	1.83
Maximum rating	65 w/mm

power levels. It has been assumed that the Doppler effect obeys a $\ln T$ law, where the temperature is the average pin temperature.

Each region was weighted with the flux and adjoint. Both were taken proportional to the calculated power profiles of Fig. 3.2 and Fig. 3.3.

The Doppler coefficient was then adjusted to fit the calculated Doppler feedback to the experimentally determined effect of 1.84 β for Core I. Thus we obtained a Doppler coefficient of $A_D = -2.3 \pm .3$ for Core I and $A_D = -1.8 \pm .3$ for Core II.

A different approach for the evaluation of the Doppler coefficient in Core I is described in /6/. In this approach, an analytical relation between effective fuel temperature and reactor power was used, which was based on an analytical approximation for the dependence on temperature of the fuel thermal conductivity. The results for A_D are very similar to those quoted above when the same ratio between effective temperature and average fuel temperature is used.

3.5 Error Analysis

The experimental Doppler feedback as a function of power had a different profile than the calculations indicate (Fig. 3.4). This could not be explained by the restructuring of the fuel. A steady loss of reactivity in the rise to power had been observed during the course of the SEFOR tests. This and the different profile

might be explained by a closing of the gap. The build up of fission gas pressure has been proposed as a mechanism that closes gradually the gap /5/. Additional uncertainties in the calculated profile of the relation between Doppler feedback and power may be caused by possible deviations from the $\ln T$ law and by other calculational uncertainties. In order to check the effect of gap closure we have assumed that no gap exists and obtained the lower curve in Fig. 3.4. The Doppler coefficient has been adjusted by 5% so that the calculated feedback agrees with the experimentally obtained value at 20 MWth. It is difficult to define correctly a gap in the case that the fuel is cracked. We feel it is reasonable to take the curves of Fig. 3.4 as upper and lower boundaries of the Doppler feedback effect.

Results of an error analysis are summarized in Table II.

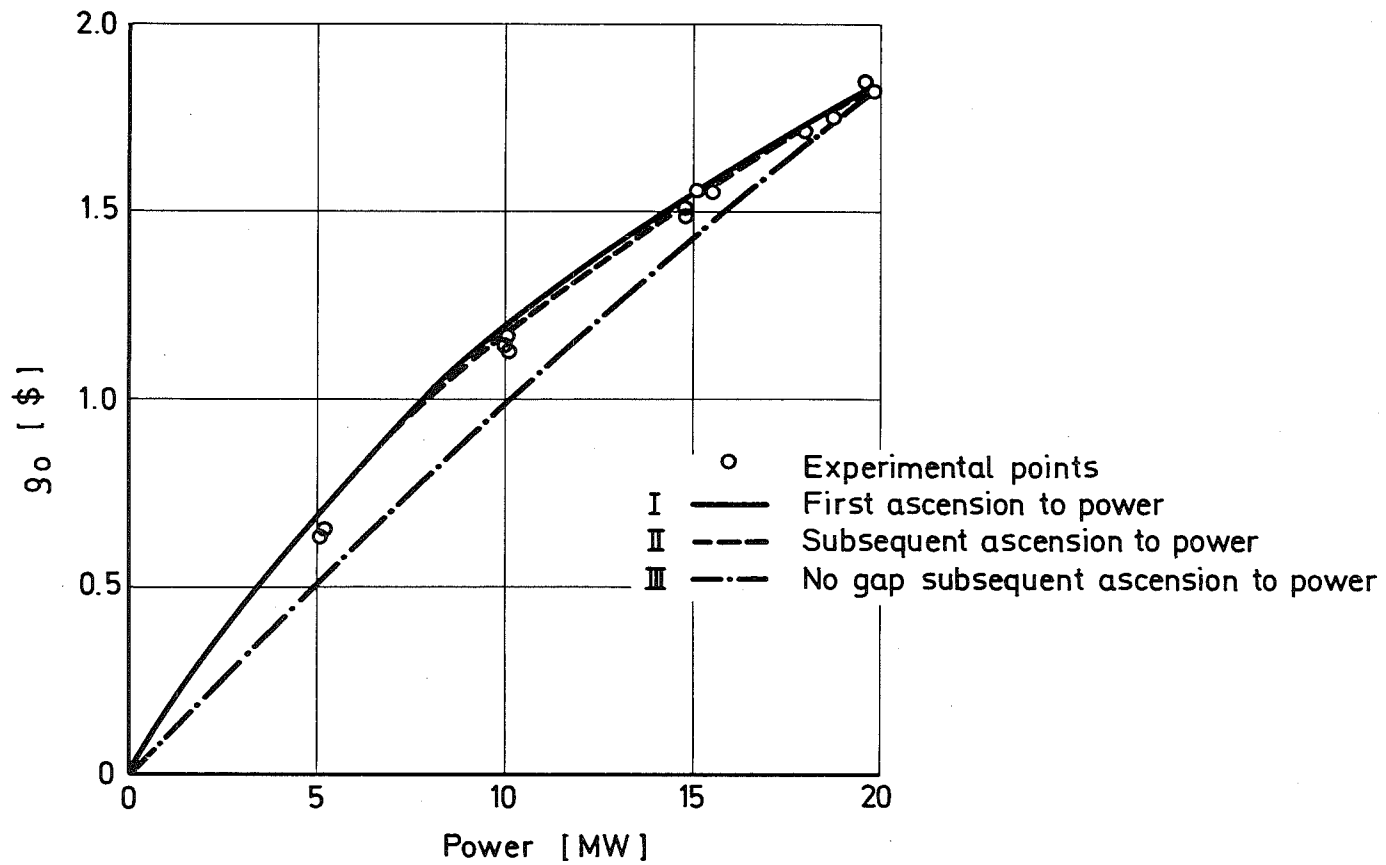


Fig. 3.4 Doppler Feedback as Function of Power for Core I

Table II Summary of Error Analysis Results⁺⁾ for
Doppler Evaluation from Static Tests

Absolute	
Absolute power	4%
Non Doppler feedback	4%
Reflector calibration errors	4%
Changes in pellet structure + gap	4%
Thermal conductivity	8%
Uncertainty in oxide to metal ratio	5%
Uncertainty of density variation	4%
Global weighting	5%
	14%

⁺⁾ Uncertainties estimated for a confidence level of ~ 90%

References for Section 3

- /1/ L.D. Noble et al.
SEFOR, Core I Test Results to 20 MW
GEAP-13702 (1971)
- /2/ G.R. Pflasterer et al.
SEFOR Development Program
31st Report, GEAP-10010-31 (1972)
- /3/ H. Kaempf, G. Karsten
Nucl. App. Techn. 9, 288-300 (Sept. 1970)
- /4/ H.E. Schmidt
Die Wärmeleitfähigkeit unbestrahlter keramischer Brennstoffe
KFK-1400 (Okt. 1971)
- /5/ H. Kaempf: Private Communication
- /6/ H. Bogensberger, L. Caldarola, F. Mitzel, D. Wintzer
Analyse der statischen Leistungsmessungen und der konventionellen Oszillatorexperimente
KFK-1271/1 (1971) - Section 1216 SEFOR

4. Analysis of the Transient Tests

4.1 Summary

The transient tests were undertaken to obtain an accurate measurement of the Doppler energy coefficient in a representative reactor environment, and to provide a convincing demonstration of its effectiveness in limiting the energy release in an LMFBR power excursion. In this chapter the analysis of the transients is presented. The results are summarized in Table I for the evaluated Doppler constants, neutron generation times l and for the average decay constant $\bar{\lambda}$ of delayed neutrons. Details of the experiments and evaluations of GE have been published in /1-3/.

Table I

	A_D	l/β	$\bar{\lambda}$ (sec ⁻¹)
Core I	$2.67 \pm .2 \text{ \$}$	$.16 \pm .01 \times 10^{-3}$	$.625 \pm .02$
Core II	$1.82 \pm .2 \text{ \$}$	$.13 \pm .01 \times 10^{-3}$	$.625 \pm .02$

4.2 Description of the Tests

In these tests the reactor power was brought to an initial steady state power level to establish representative fuel rod temperature distributions, whereupon a B_4C rod was ejected from the core in approximately .1 seconds /1/. The resulting power transients were moderated by the Doppler reactivity until a delayed scram terminated the tests at ~ 300 msec. A series of subprompt tests was run for each core prior to the ejection of B_4C rods with reactivities greater than 1 β . Typical results are shown in Fig. 4.1 and Fig. 4.2.

4.3 Outline of the Analysis

Inverse kinetics has been the basis to calculate from the changes in power the net reactivity. A cell model has been used to calculate temperature distributions in the fuel, clad, coolant and fuel element boxes. The sum of the net reactivity and calculated feedback reactivity were required to remain constant after full ejection of the boron slug and before the delayed scram. For non Doppler feedback reactivities calculated values were used. The Doppler constant was adjusted so that the requirement was fulfilled. It was found that the Doppler constant was quite sensitive to the assumed value of the average decay constant of the delayed neutrons. This latter value could be determined using the sub- and superprompt transients. The inserted reactivity should be a smooth function of time during the ejection of the boron rod. This enabled a determination of the reduced lifetime of the neutrons in the reactor.

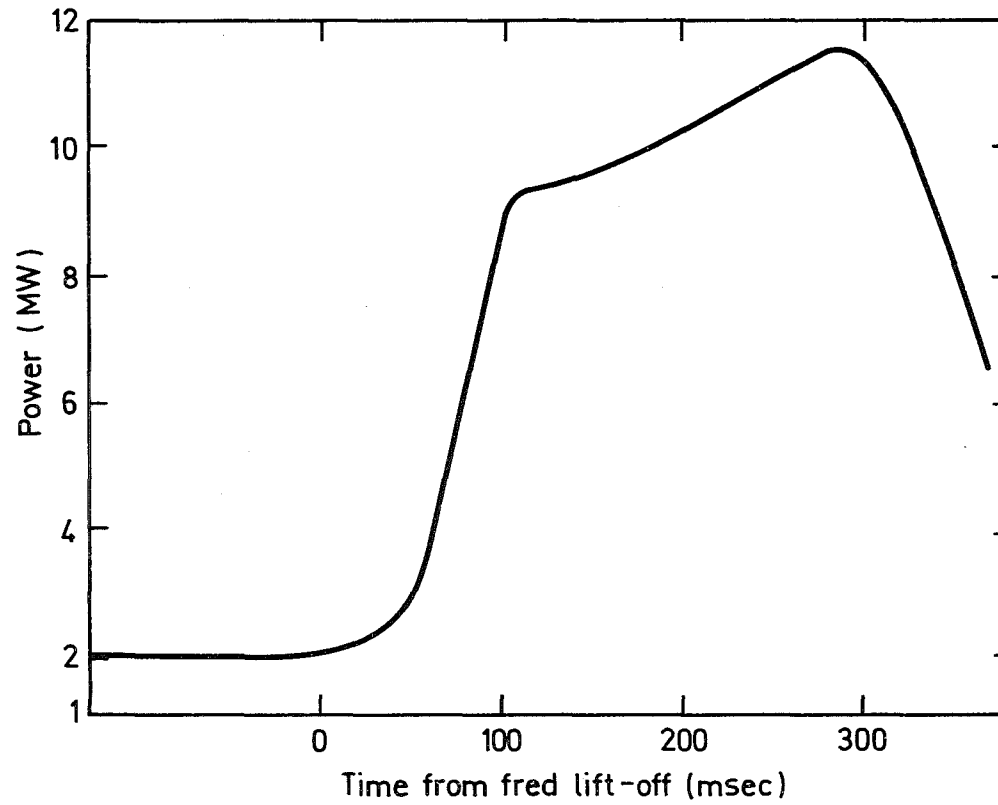


Fig.4.1 Time Dependent Power for Sub-Prompt Transient 2
Core II

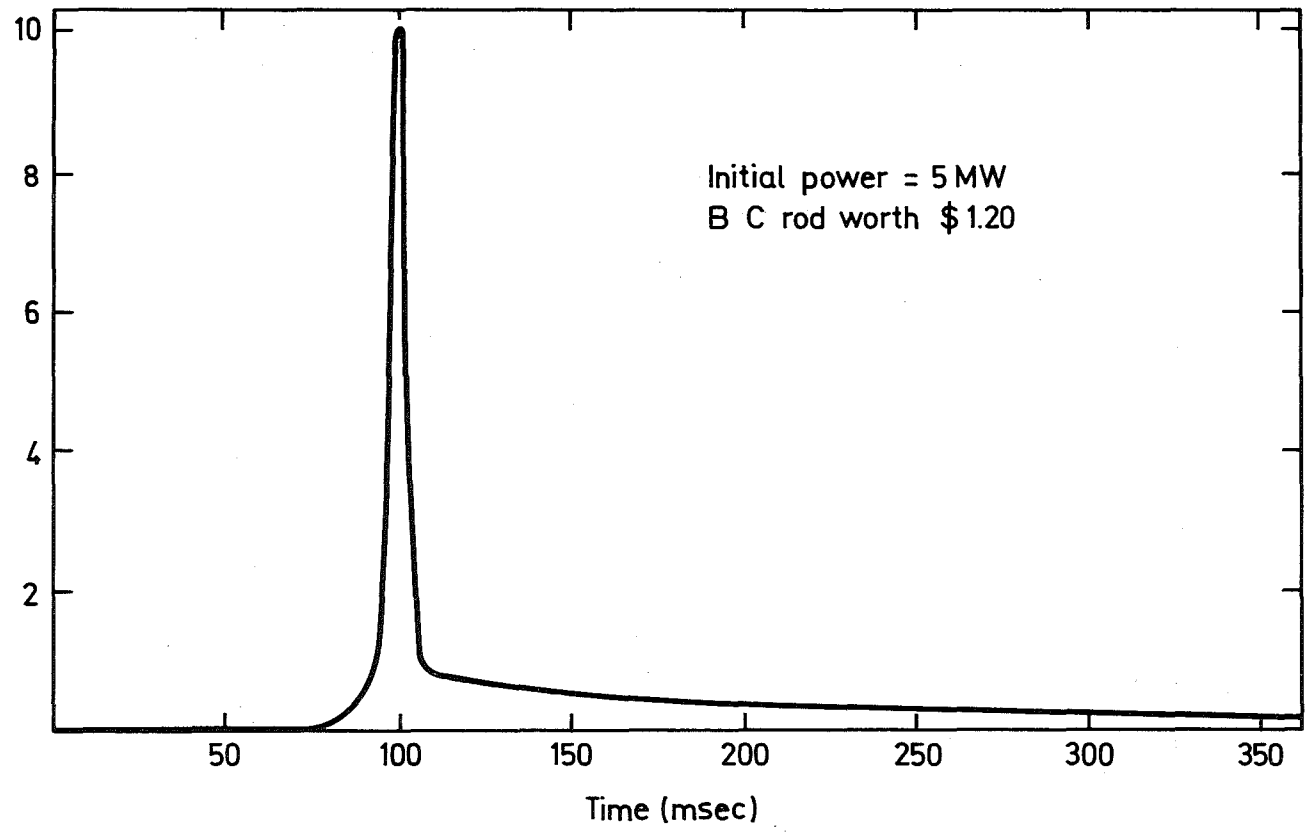


Fig. 4.2 Core II Super - Prompt Transient

4.4 Inverse Kinetics

The inverse kinetics equation for a point reactor model in the integral form is given by (2):

$$\rho_n = 1 - \frac{P_o}{P(t)} + \frac{\Lambda}{\beta} \cdot \frac{1}{P} \frac{dP(t)}{dt} - \frac{1}{P} \int_0^t (P(t) - P_o) \sum_{i=1}^6 a_i \lambda_i e^{-\lambda_i(t-t')} dt' \quad (1)$$

- where ρ_n = net reactivity
 P = power
 P_o = power at the beginning of the experiment
 β = effective delayed neutron fraction
 Λ = effective neutron lifetime
 a_i = effective fraction of the delayed neutrons of the group i
 λ_i = decay constant of the precursor nuclei of the group i

The net reactivity is the sum of the inserted (by B_4C rod ejection) reactivity ρ_{in} and the (negative) feedback reactivity ρ_{fb} . The first two terms of Eq. (1) form the familiar prompt jump approximation. The third term is the reactivity contribution due to the neutron lifetime, it is important only for superprompt tests. The last term is the contribution of the delayed neutrons.

The computer analysis of recorded power traces was based on Eq. (1) without introducing further simplifications.

4.5 Feedback Effects

The feedback is caused by the Doppler feedback and expansion effects of the core. The core has been specifically designed to study the Doppler effect and the expansion effects were therefore kept to a minimum.

The calculation of expansion effects requires a temperature distribution of all the components fuel, clad, coolant and fuel boxes. A rough knowledge is however only required as the effects are small. We have taken special care to obtain a fair approximation of the time dependence of the expansion effects. We require as outlined in 4.4 that the sum of net reactivity and feedback reactivity remains constant after full ejection of the boron rod. This means that errors in the time dependence of the expansion effect will be compensated by the Doppler coefficient, enhancing the errors in the Doppler determination. The time constant for the fuel is fortunately of the order of 30 sec. The fuel element boxes have however a time constant of ca. 50 msec. Heating of the boxes results in bowing of the fuel elements due to the clamping and results in a sizeable reactivity effect. We have therefore made a cell calculation (Fig. 4.3) with four zones: fuel, clad, coolant and structure.

The temperature distribution is given by

$$\frac{\partial T}{\partial t} = a \operatorname{divgrad} T + \frac{Q}{c} \quad (2)$$

where $a = \frac{\lambda}{c}$ is the thermal diffusivity
 c is the heat capacity
 λ is the thermal conductivity
 Q is the deposited power density

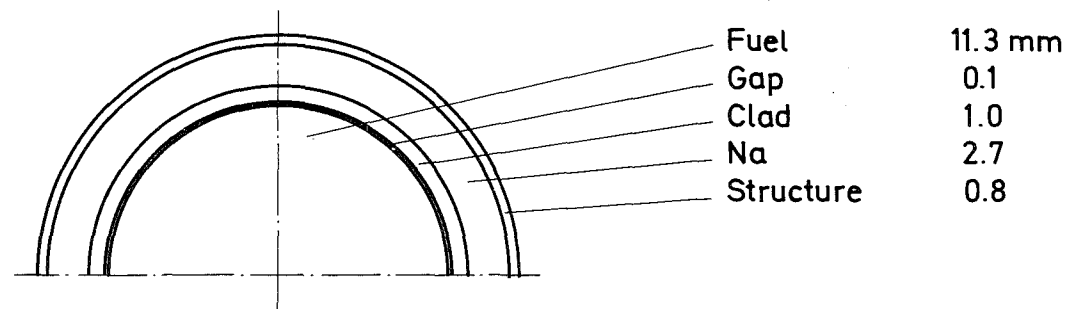


Fig. 4.3 Dimensions used for Cell Calculations

The energy deposition in the different zones is given in Table II. Table III contains the volume fractions and specific weights. Table IV shows data used for heat capacity and thermal conductivity. For this evaluation a less refined model and more approximate values for the heat conductivity have been used than in the static tests.

In Fig. 4.4 we have depicted two temperature profiles. From the temperature distributions average fuel, clad, coolant and structural material temperatures were calculated. From the average temperature rise the time dependent non Doppler effects were calculated with the values of Table V.

4.6 Determination of the Average Decay Constant of the Delayed Neutrons

In order to simplify the argumentation, we consider simplifications (compare /10/ and /11/) of Eqs. (1) and (2). (In the actual evaluations the full equations have been used):

The approximation of the term $e^{-\lambda_i(t-t')}$ in the integrand of (1) by 1.0 introduces little error during the duration of the experiment (~ 300 msec) since the effective decay time of the delayed neutrons is about 2 sec. Eq. (1) simplifies to (3) if we further neglect the term $\frac{\Lambda}{\beta} \frac{1}{P} \frac{dP(t)}{dt}$, which is small compared to the other terms except during the short time period of superprompt criticality in the superprompt transient experiments.

Table II SEFOR Energy Deposit in MeV/Fission

	Cell	Fuel	Steel	Na + BeO	Out- side Core
Kinetic energy fission products	168.	168.	--	--	--
Prompt γ from fission	7.50	6.90	.48	.12	--
Prompt capture γ 's	7.50	6.30	.93	.27	--
γ from inelastic scattering	3.27	3.09	.15	.03	--
Elastic scattering	.66	.58	.06	.16	1.74
Prompt sum	186.93	184.87	1.62	.58	1.74
Delayed β 's	7.0	7.0	--	--	--
Delayed γ 's	6.0	\sim 5.0	\sim .70	\sim .30	--
Total	199.93				
Prompt zone / total	.935	.924	.0081	.0029	

Table III

Volume Fractions and Specific Gravity

	Vol fraction	Sp gr	Total mass	Fractional energy deposit / kg
Fuel	.432	10.0 ⁺⁾	2150	429. x 10 ⁻⁶
SS	.213	7.83	830	.975 x 10 ⁻⁶
Na + BeO	.352	.97	171	17.5 x 10 ⁻⁶

⁺⁾ .92 of theoretical density

Table IV Heat Capacity and Thermal Conductivity

Material	Heat capacity cal/9°C	Thermal conductivity
Fuel	$.0669 + 1.125 \times 10^{-5} T^{*})$	$.015 - 1.47 \times 10^{-5} xT + 4.96 \times 10^{-9} T^2 \text{ *)}$
Gap	--	.286
SS	.12	.035
Na	.305	45.0

*) Average fuel temperature has been used

Table V Non Doppler Feedback Coefficients

Axial clad expansion	.0013 $\$/^{\circ}C$
Radial core expansion	.0027 $\$/^{\circ}C$
Axial fuel expansion	.0002 $\$/^{\circ}C$

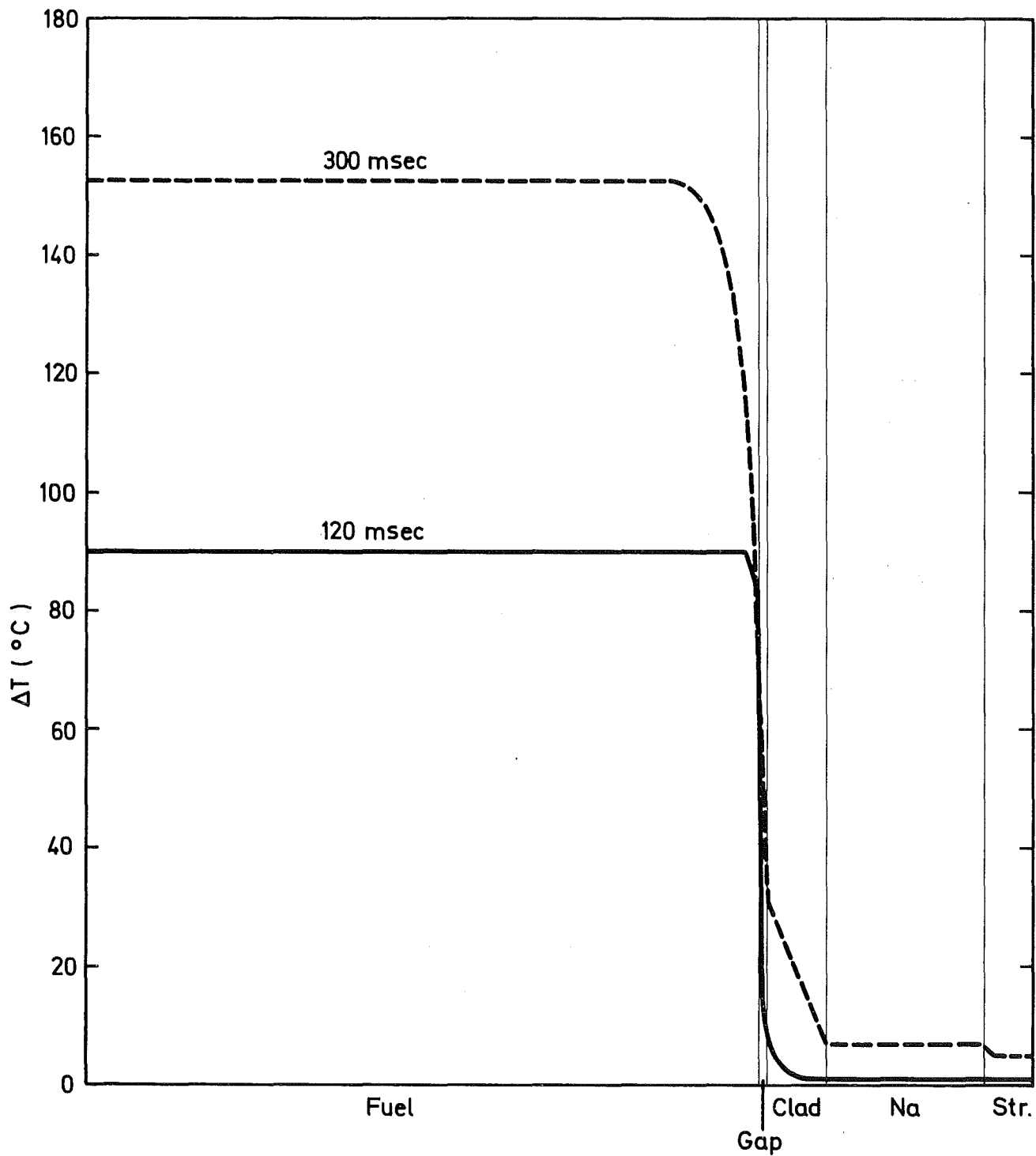


Fig. 4.4 Temperature Rise in SEFOR I Super 2

With this exception, a good approximation to Eq. (1) is:

$$\rho_n(t) = 1 - \frac{P_o}{P(t)} - \frac{\bar{\lambda}}{P(t)} \cdot E(t) \quad (3)$$

where $\bar{\lambda} = \sum_{i=1}^6 a_i \lambda_i$ is the average decay constant of the delayed neutrons and

$$E(t) = \int_0^t (P(t') - P_o) dt' \text{ is the transient energy}$$

In an adiabatic situation Eq. (2) becomes:

$$\frac{\partial T}{\partial t} = \frac{Q}{c} \text{ or } T_x = T_{ox} + \frac{q_x}{c_x} \cdot E(t) \quad (4)$$

where q_x is the heat deposit per MJ reactor energy per kg of the zone x

We assume furthermore that the Doppler feedback and the non Doppler feedback can be described by a linear function of the temperature rise

$$\rho_{fb} = E(t) \sum_x \frac{a_x}{c_x} = \gamma E(t) \quad (5)$$

where ρ_{fb} = is the feedback reactivity

a_x = is the feedback coefficient for the zone x.

The inserted reactivity is then given by

$$\rho_{in} = \rho_n(t) + \rho_{fb}(t) = 1 - \frac{P}{P_0} - \frac{\bar{\lambda}}{P} E + \gamma E \quad (6)$$

This equation demonstrates that the evaluation of the Doppler energy coefficient γ by analysis of ρ_{in} , P and E is complicated by the term $\frac{\bar{\lambda}}{P} E$ and that an error in $\bar{\lambda}$ leads to an error in γ .

Information about both, $\bar{\lambda}$ and γ (or the related quantity A_D), can be obtained by analysis of different transient experiments with different ranges for $\bar{\lambda}/P$.

We combined four tests of Core II to increase the accuracy (Table VI). All tests had an initial power of 2 MW. Two data channels were used for each test. For each test γ was determined for a fixed average decay constant. The results are shown in Fig. 4.5. We obtained an average decay constant for the delayed neutrons of $\bar{\lambda} = .625 \pm .02$. The calculated value using Keepin's data /6/, is $\lambda = .57 \pm .06$, which is about 10 per cent less than .625.

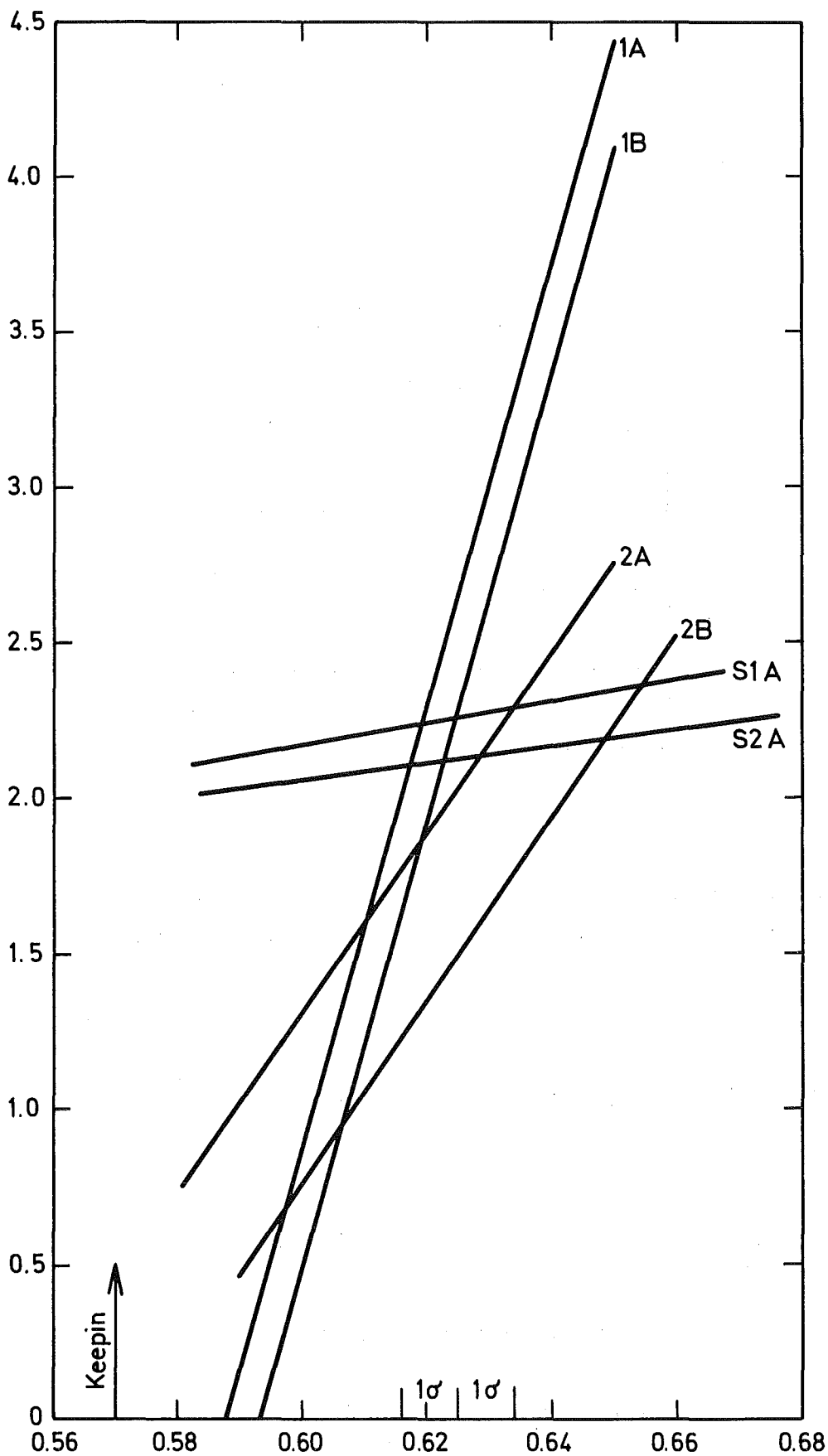


Fig. 4.5 Feedback Coefficient versus Average Decay Constant

Table VI Tests Used for the Determination of the Average Decay Constant

Test name	Max. reactivity
B 1	.5 \$
B 2	.8 \$
S 1	1.12 \$
S 2	1.18 \$

The uncertainty of the calculated value was estimated assuming that we have only fissions in ^{239}Pu and ^{238}U , which is fairly correct

$$\bar{\lambda} = \left(1 - \frac{F_8}{F_9 + F_8}\right) \frac{\beta_9}{\beta_{\text{eff}}} \cdot \bar{\lambda}_9 + \frac{F_8}{F_9 + F_8} \cdot \frac{\beta_8}{\beta_{\text{eff}}} \cdot \bar{\lambda}_8 \quad (7)$$

where F_x = is the fission rate of nuclide x

$\bar{\lambda}_x$ = is the corresponding average decay constant

β_x = is the fraction of the delayed neutrons for fissions in nuclide x

β_{eff} = is the effective fraction of the delayed neutrons in the reactor

The decay constants of ^{238}U and ^{239}Pu are fairly different (Table VII).

Table VII Effective Decay Constants

^{238}U			^{239}Pu		
λ_i	a_i	$a_i\lambda_i$	λ_i	a_i	$a_i\lambda_i$
0.0132	0.13	.00017	.0129	.038	.0005
.0321	.137	.00440	.0311	.280	.0087
.139	.162	.02252	.134	.216	.0289
.358	.388	.13890	.331	.328	.1086
1.41	.225	.35955	1.26	.103	.1298
4.02	.075	.30150	3.21	.035	.1124
sum		.827			.3888

Expression (7) leads to a $\bar{\lambda}$ uncertainty of 10 per cent when the estimation is based on the following partial uncertainties:

- 7% in the fission ratio
- 7% in the contribution of ^{239}Pu to β_{eff}
- 7% in the effective decay constant for the isotopes /6/.

4.7 Determination of the Reduced Neutron Lifetime $1/\beta$

The inserted reactivity is known from static reactivity measurements (compare /7/, p. 6 - 74) to be a smooth function of position and hence a smooth function of time. When the inserted reactivity is calculated from power traces of the transient experiments using Eq. (1) and Eq. (6), it is fairly sensitive to the reduced neutron lifetime in the region between 80 and 120 msec (Fig. 4.6). Visual inspection of reactivity plots with different reduced neutron lifetimes gave the following values.

	<u>GfK</u>	<u>ORNL noise /7/</u>
Core I	.16 \pm .01 msec	.13
Core II	.13 \pm .01 msec	.14

They compare well with the GE values but differ markedly from the ORNL measurements. This might well be caused by the effects of the reflectors on the lifetime. ORNL has measured at low power with the reactor below critical. The transients were performed with nearly all the reflectors in.

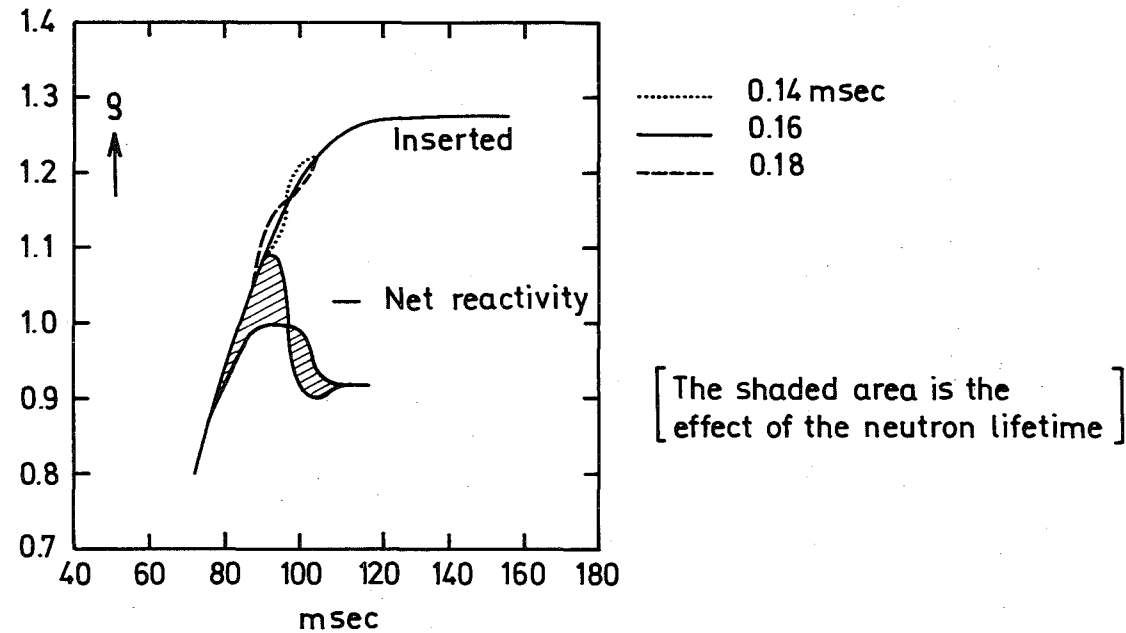


Fig. 4.6 Core I Transient No. 2
Effect of the Neutron Lifetime

4.8 Doppler Evaluation

The full Eq. (1) and the temperature model of 4.5 were used to determine the Doppler coefficient. The temperature model described in 4.5 is more exact than the usual adiabatic approximation because it includes effects of heat conduction on the development of the temperature pattern in a fuel rod cell (compare Fig. 4.4). These effects were found to be not negligible for the interpretation of the transient experiments.

The calculational procedure for the Doppler coefficient determination for each experiment included the steps:

- Temperature calculations for fuel rod cells for different amounts of transient energy depositions (to describe different positions in the core) with the same time development of the energy deposition as derived from corresponding experimental power traces.
- Doppler- (based on an $\ln T$ law) and non Doppler feedback calculations.
- Flux and adjoint flux weighting of the results for different positions in the reactor, where the energy deposition was assumed to be proportional to the flux.
- Comparison of the results with the results of feedback reactivity calculations obtained from Eq. (1) and application of a least square fit procedure for determination of the Doppler constant.

Table VIII presents the results of the Doppler constant determination for several transient experiments in Core I and Core II.

Table VIII Doppler Constant Determination

Transient number	Initial power (MW)	A_D	
Core I			
1	2	2.60	} $2.67 \pm .2$
2	2	2.52	
4	5	2.60	
5	5	2.67	
6	10	2.82	
7	10	2.81	
Core II			
1	2	1.84	} $1.82 \pm .2$
2	2	1.74	
4	5	1.88	

4.9 Error Analysis and Discussion

Table IX summarizes the results of an error analysis for the determination of the Doppler constant from transient experiments. Our results are comparable to the analysis results of GE and HEDL /8/. It should however be noted that the agreement is partially accidental as our analysis differs in several details. Some of the more important differences between GE and our analysis are given in Table X. Special care has therefore to be taken should these results be used to normalize predictions of the Doppler effect that the same methods are used as given in this chapter /9/.

Table IX Results of uncertainty⁺⁾ estimates for the evaluation of the Doppler coefficient from transient experiments

Noise of signal and non linearity of amplifiers	4%
Absolute power	5%
Non Doppler feedback	5%
Decay of delayed neutrons	7%
Specified heat of the fuel	8%
Global temperature weighting	4%
Thermal conductivity and gap coefficient	3%
β_{eff}	10%
Total	16%

⁺⁾ estimated for a confidence level of $\sim 90\%$

Table X Model Differences for Doppler Coefficient
Determination

	KA	GE	δA_D
Prompt energy released in the fuel	92.4%	88%	- 5%
Average decay constant for the delayed neutron precursors	.625	.572	+ 8%
Linearity between Doppler and non Doppler feedback	no	yes	- 8%
lnT weighting over the pellets	no	yes	- 4%
Difference in reference temperature at the beginning of the transient			2%

References for Section 4

- /1/ Topical reports GEAP 13837 SEFOR Core I Transients

- /2/ Topical reports GEAP 13838 Experimental program re-
sults in SEFOR Core II

- /3/ Quarterly reports GEAP 10010 - 1 - 31

- /4/ E.R. Mc Keehan

Design and Testing of the SEFOR fast reactivity excu-
sion device (FRED)
GEAP 13649

- /5/ S.G. Carpenter

Nucl. Sci. and Eng. 21, p. 429 (1965)

- /6/ G.R. Keepin

The physics of nuclear kinetics
Addison Wesley, 1965

- /7/ GEAP 10010 - 31

/8/ R.A. Harris

Application of the result of the SEFOR Doppler experiments to the FTR

Trans. Act. of the ANS Vol. 16, p. 281
Chicago, June 1973

/9/ L. Caldarola et al.

SEFOR results and application to LMFBR's

International Conference on Engineering of Fast Reactors for Safe and Reliable Operation, Karlsruhe, F.R.G.,
9 - 13 October 1973

/10/ W. Häfele

Prompt überkritische Leistungsexkursionen in schnellen Reaktoren

Nukleonik, Band 5, Heft 5 (1963)

/11/ K. Ott

Theorie verzögert überkritischer Exkursionen zur Messung der Doppler-Koeffizienten

Nukleonik, Band 5, Heft 7 (1963)

5. Analysis of Oscillator Experiments

This section summarizes results of the analysis of SEFOR oscillator experiments and experiences obtained during the analysis. A detailed description of dynamical models developed for and used in the analysis is published elsewhere /1/, /2/.

Conventional oscillator experiments (C.O.E.) and two kinds of balanced oscillator experiments have been performed one with the coolant temperature (I.B.O.E.) and the other with the reactor power kept constant (II.B.O.E.).

The analysis of the I.B.O.E. showed that a better interpretation of the measured data was possible by taking into account the temperature dependence of the fuel to gap heat transfer coefficient h_g . This can be clearly demonstrated with the transfer function between coolant flow and power. The fit to the experimental points, plotted in Fig. 5.1, is much better in the case in which the temperature dependence of h_g ($K = 0.3$) was taken into account than in the case in which this dependence was neglected ($K = 0$).

The fuel time constant τ has been determined from the transfer function between power and reactivity. The results are in good agreement with corresponding calculations as shown in Table I. This table includes also the data evaluated by GE.

The results of the B.O.E. agree very well, the small differences being probably due to the different models. The different calculated results are due to the different evaluation methods. The bigger value results from a thermal resistance calculated with a linear interpolation, whereas the smaller value is obtained by the using the tangent for the thermal resistance. The latter method is

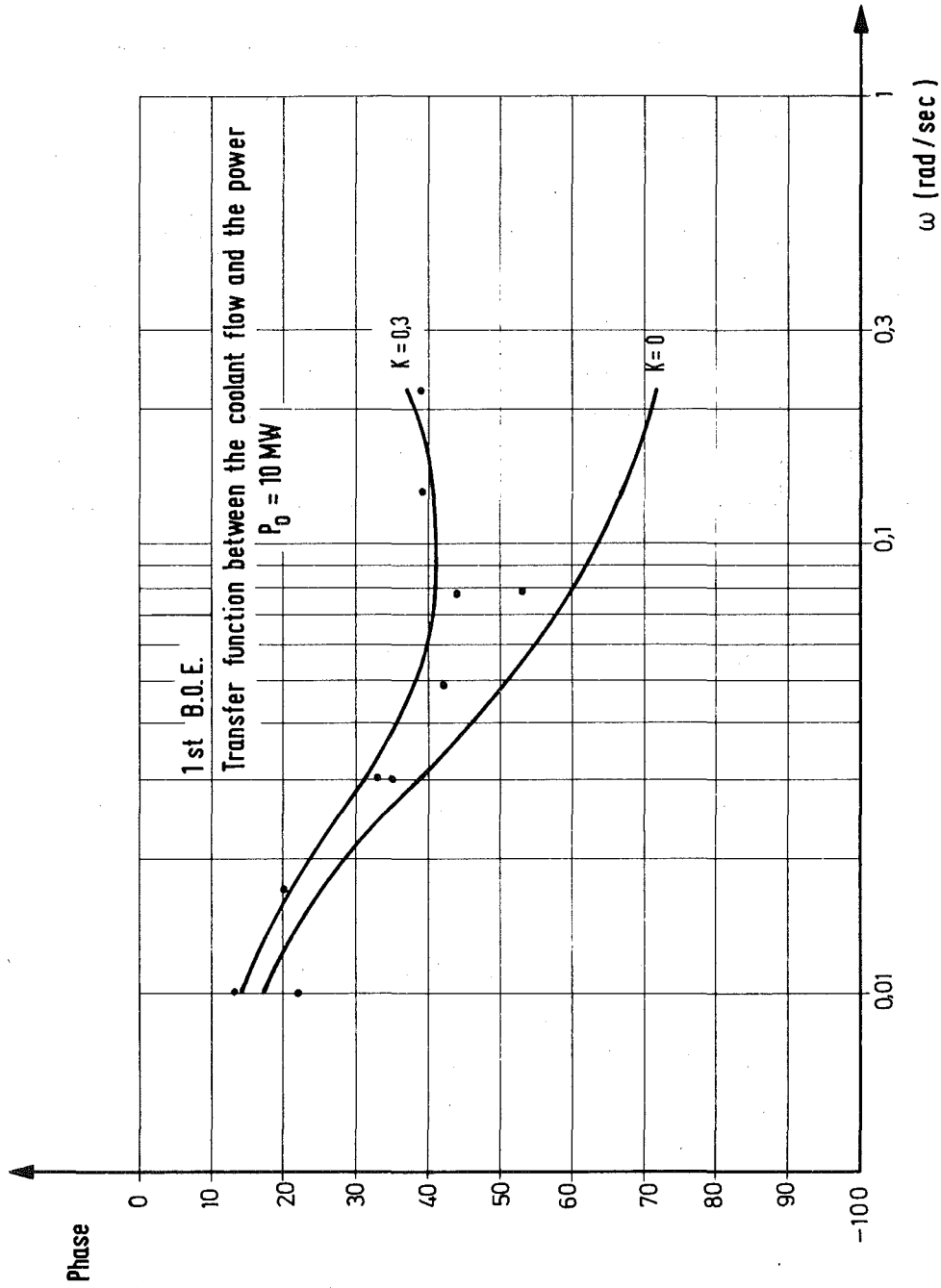


Fig. 5.1

Table I Fuel Time Constants Evaluated from Oscillator Experiments

P _o (MW)	$\bar{\theta}_o$ (°F)	Fuel time constant (sec)				
		GE			GfK	
		Conv.	B.O.E.	Calc.	B.O.E.	Calc.
10	560		27.1		27.7	26.7
19	760	24.5	22.1	26.5	19	19.7

$$\text{GE} \quad \tau = \frac{T_{av} - \theta_o}{P_o} V_f \rho c$$

$$\text{GfK} \quad \tau = \frac{\delta T_{av}}{\delta P_o} V_f \rho c$$

- T_{av} = average fuel temperature
- θ_o = average sodium temperature
- V_f = volume of fuel
- ρ = density of fuel
- c = heat capacity of fuel

more correct and agrees much better with the I.B.O.E. However the results of the C.O.E. remain still different from those of the I.B.O.E. and of the calculations. A similar situation is reflected in the results of the Doppler power coefficient shown in Table II.

This table compares values for the Doppler power coefficient evaluated by GE and GfK.

Table II Doppler Power Coefficient Results

P _o (MW)	$\bar{\theta}_o$ (°F)	Doppler power coefficient (¢/MW)				
		GE			GfK	
		Conv.	B.O.E.	Calc.	B.O.E.	Calc.
10	560		9.65		9.55	9.3
19	760	4.2	4.9	5.1	4.8	4.9

From a comparison of the static experiments, the C.O.E. and the I.B.O.E. it appears very clearly that the results of the I.B.O.E. agree with those calculated from the static tests much better than with those from the C.O.E. This may be explained by the existence of a reactivity structure coefficient with a very long time constant which has already been attenuated at the frequencies used for the oscillator experiments.

Since the coolant temperature was kept constant, both in the I.B.O.E. and in the static tests, the results of these tests are not affected

by this hypothetical structure coefficient, whereas the conventional oscillator experiments are affected. The structure coefficient, used in the analysis of the C.O.E., was obtained from the static tests. As no attenuation was included in the model, this effect was practically overcompensated in the analysis. Qualitatively this conclusion holds also for the results of the II.B.O.E.

During the 2nd B.O.E. it was first tried to keep the power constant by oscillating the reactivity and the primary flow. However it was observed that, at low frequencies, inlet and outlet temperatures were in opposition of phase so that the amplitude of the reactivity oscillations was very small and the Doppler coefficient could not be evaluated in this way. This effect is due to the delay constants of the primary loop. This result is confirmed by the calculations carried out with the SEFAN code (Fig. 5.2). Here the amplitude of the average reactor coolant temperature $((T_i + T_o)/2)$ is shown as a function of the frequency. This amplitude is low at lower frequencies and high at higher frequencies, due to the different phase between outlet and inlet temperature. It was then tried to keep the inlet coolant temperature constant by oscillating the secondary flow.

However, due to the large thermal capacity of the structure between core outlet and reactor outlet, the temperature oscillations at reactor outlet are strongly attenuated and this effect did not allow a good control of the reactor inlet temperature by means of the secondary flow.

All results of the oscillator experiments are of general importance because of their direct relation to general questions of reactor stability and plant dynamic behaviour. The analysis of the C.O.E. and the B.O.E. showed that the plant dynamic behaviour including the coolant systems is well understood. This confirms the accuracy of the analytical model and the calculational methods used and gives confidence in its application to other LMFBR's.

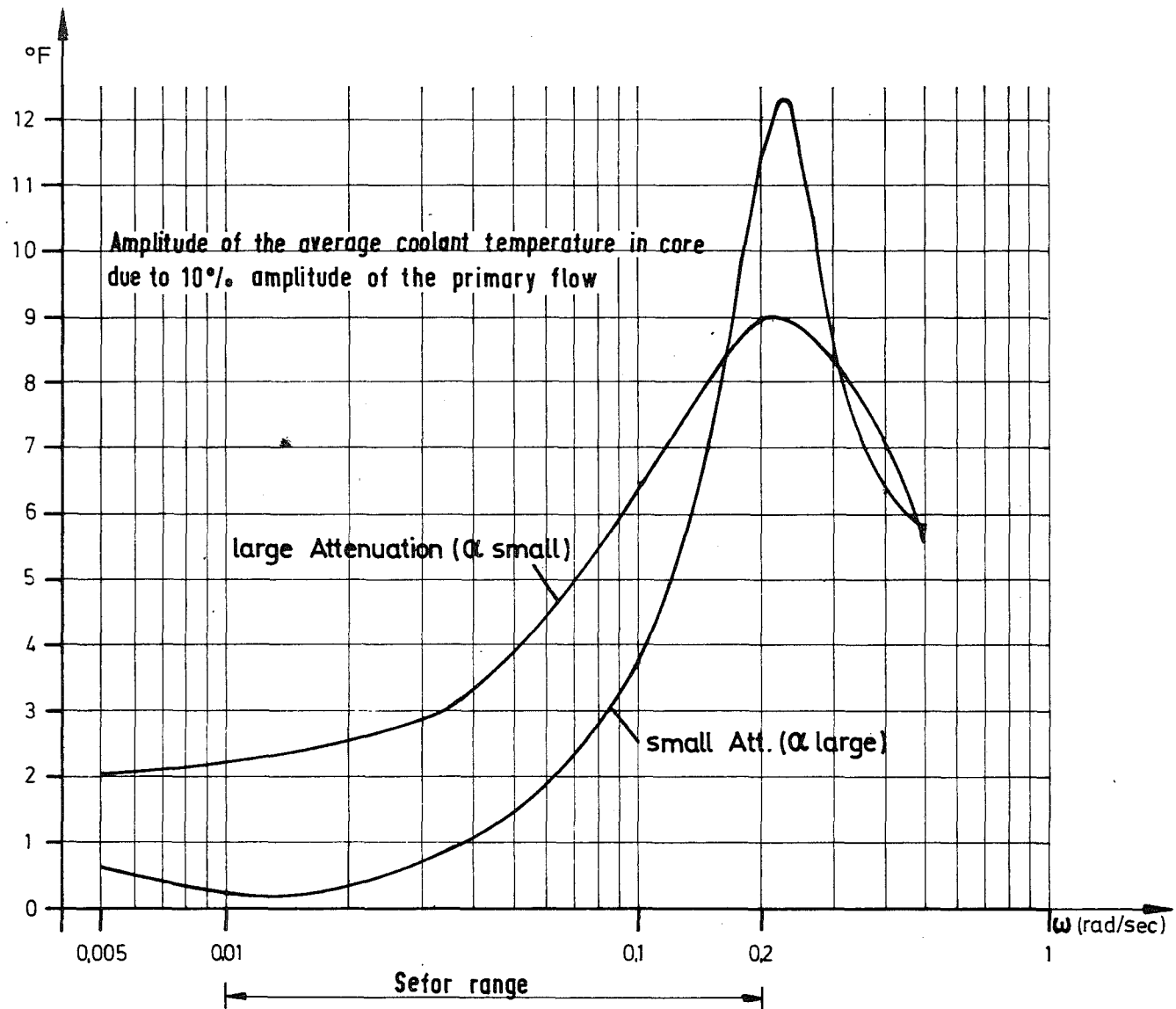


Fig. 5.2

References for Section 5

/1/ L. Caldarola, P. Ferranti, F. Mitzel

Fast Reactor Transfer Functions with Special Reference
to the Nonlinearities and to the Spatial Dependence of
the Heat Transfer Process

KFK-2027 (1974) (Topical Report)

/2/ L. Caldarola, P. Ferranti, F. Mitzel

Fast Reactor Transfer Functions with Special Reference
to the Nonlinearities and to the Spatial Dependence of
the Heat Transfer Process

(to be published in Nuclear Technology)

6. Nuclear Doppler Calculations

6.1 Summary

Calculated results for $A_D = -T \, d\rho/dT$ are
 $A_D = 8.4 \cdot 10^{-3}$ for Core I
and $A_D = 6.3 \cdot 10^{-3}$ for Core II.

These numbers were obtained with the MOXTOT cross section set.
KFKINR results are lower by about 5 per cent.

Agreement with experimental numbers is within the range of experimental uncertainty, with a slight preference for the KFKINR set.

Numerical studies demonstrate the importance of sufficiently detailed geometrical models and of the application of several corrections for Doppler calculations. Several questions are discussed concerning the calculation of the temperature dependence of effective group cross sections.

6.2 Studies Concerning the Temperature Dependence of Effective Cross Sections

The calculation of effective resonance capture and fission cross sections for the temperature range in question is one of the principle steps in nuclear Doppler calculations.

The straight forward way to perform this step with the present GfK code system is the use of the interpolation routine /1/ for shielded cross sections (f-factors), which are tabulated for the temperatures 300^oK, 900^oK, and 2100^oK.

Questions arise about possible errors of the interpolation procedure and about possible errors in the calculation of self-shielding factors at the reference temperatures.

Concerning the first question, comparison calculations were performed for the Doppler coefficient of SEGOR 1-D (reactivity differences based on perturbation theory) with

- a) using the interpolation routine /1/, and
- b) using the DOPRO /2/ code

with the major difference, that b) avoids errors of interpolation. The difference of the results was found to be less than 2 per cent (.00785 for b) and .00770 for a)), which is considered to be negligible compared to other possible errors.

Regarding the second question, information was gained by a comparison between DOPRO and RABID /3/ calculations; with the same input of nuclear resonance parameters. The methodical difference is, that DOPRO is based on the "Narrow Resonance" (NR) approximation, while the more elaborate RABID code numerically, and more generally, treats the more complicated moderation effects occurring mainly in wider resonances.

Table I permits a comparison of results /4/ for individual ²³⁸U resonances:

Table I Comparison of NR with RABID Results for Effective ^{238}U Capture Cross Sections

(Differences Between Resonance Integral Contributions δRI for 500°K and 1100°K in 10^{-3} Barns)

E [ev]	Γ_n [ev]	δRI (500°K - 1100°K)		Relative Difference
		NR	RABID	
1802	0.670	0.7	0.73	4%
1710	0.646	2.0	2.1	5%
1255	0.236	2.6	2.77	6.5%
793	0.0024	0.50	0.53	6%
697	0.057	9.5	10.0	5%
584	0.026	12.4	12.73	3%

Condensed information is presented in Table II for those energy groups, which predominantly contribute to the Doppler effect.

Table II Comparison of NR with RABID Results for Three Important Energy Groups

Energy Group	$\delta\sigma_c$ (500°K - 1100°K)	
	[b]	
	DOPRO	RABID
2.15 - 1.0 keV	0.103	0.105
1.0 - 0.465 keV	0.184	0.202
0.465 - 0.215 keV	0.209	0.233

It can be estimated from Table I and Table II (by extrapolating the results of these tables to other, less important energy groups), that a "non-NR") correction of about 5% should be applied to calculated NR results for the Doppler coefficient for SEFOR.

An other study using the DOPRO /2/ code gives information about the relation between uncertainties of the SEFOR Doppler coefficient and uncertainties of the p wave strength function S_1 . The range of numerical values in discussion is about $1.5 \cdot 10^{-4} < S_1 < 2.5 \cdot 10^{-4}$. The SEFOR Doppler coefficient was found to be 9 per cent higher for $S_1 = 2.5 \cdot 10^{-4}$ than for $S_1 = 1.5 \cdot 10^{-4}$.

Local fuel Doppler reactivity effects are usually calculated for the average temperature of the fuel rod section in question without explicitly taking into account the radial temperature profile across the fuel rod. This approximation was checked for SEFOR rods by comparative RABID calculations. Effective ^{238}U capture cross section differences $\Delta\sigma_{c8}$ were calculated for temperature transitions (averaged over the rod cross section) from 500°K to 1000°K with

- a) specially constant temperature across the rod, and
- b) a parabolic temperature profile with the same average temperatures as in a).

The results for three important energy groups are shown in Table III.

Table III Comparison of $\Delta\sigma_{c8}$ for Flat and Parabolic Temperature Profiles

Energy Range keV	$\Delta\sigma_{c8}$ [barns]	
	without T profile	with parabolic T profile
2.15 - 1.0	.092	.091
1.0 - 0.465	.176	.175
0.465 - 0.215	.200	.197

The results of Table III demonstrate that errors due to the flat temperature approximation can be neglected in the case of SEFOR rods.

6.3 Variation of Doppler Results with Geometrical Models

The interpolation routine /1/ was used and perturbation theory was applied to obtain the Doppler coefficients listed in Table IV for differently detailed geometrical models of SEFOR I-D. Flux and adjoint distribution were calculated with MOXTOT cross sections in diffusion theory approximation.

Table IV: Doppler Results for Different Geometrical Models

Geometrical Model	$A_D = - T \, d\rho/dT$
Spherical model	.00610
Cylindrical model (with vertical bucklings)	.00670
Detailed r-z model	.00686

It can be seen that a rather detailed geometrical model of the reactor is required for accurate Doppler calculations.

6.4 Comparison of Results for Different Cross Section Sets

The comparison was based on one dimensional diffusion calculations for a spherical model /5/ of SEFOR. The MOXTOT set has been chosen arbitrarily as a basis for the comparison, the results of which are shown in Table V.

Table V: Relative Differences in Calculated Doppler Coefficients for Different Cross Section Sets

Set	$\Delta A_D/A_D$
MOXTOT	(basis)
KFKINR	- 5 %
NAPPMB	- 5 %
ABN (GfK)	- 11 %
ABN (1964)	+ 21 %
ENDF/B-II	+ 15 %
MOD.ENDF/B-II	+ 12 %
FTR III	+ 35 %

The Doppler coefficient results for the last 5 sets were taken from /5/. It can be seen that there are remarkable differences in the Doppler results for some of the sets in the table. The big difference between ABN (GfK) and the older (1964) set is essentially caused by different nuclear data for ²³⁹Pu.

6.5 Errors Introduced by the Perturbation Theory Approximation

The perturbation theory approximation neglects second order effects on the flux and adjoint distribution caused by the transition from "unperturbed" to "perturbed" cross sections. Corresponding errors can be avoided by successive criticality calculations for some discrete temperature levels.

Doppler effect calculations for SEFOR 1-D have been performed with both methods. Flux and adjoint distributions were based on one dimensional (radial) diffusion calculations. The results are well fitted by

$$T \, d\rho/dT = - A_D (T/T_0)^{-\alpha} \quad (1)$$

where $d\rho/dT$ is the temperature (T) derivative of reactivity ρ , T_0 is a reference temperature, A_D is the Doppler coefficient at T_0 and α is an exponent which in the case $\alpha \neq 0$ describes the deviation of the calculated results from a simple $\ln T$ - law for ρ . $T \, d\rho/dT$ is close to $-A_D$ when T is close to T_0 . Eq. (1) permits the translation of A_D from T_0 to other reference temperatures.

The calculations yielded $A_D = .0070$ (as expected for both methods of $\Delta\rho$ calculations) and

$\alpha = 0$ for the perturbation theory results,

$\alpha = 0.08$ for successive reactivity calculations

6.6 Additional Corrections

Perturbation theory applied to two dimensional (r,z) flux and adjoint distributions yielded $A_D = .0083$, when REMO corrected (compare section 2.2) MOXTOT cross sections were used. The corresponding result without REMO correction is $A_D = .0075$. Both values refer to core I-D and to a Doppler reference temperature $T_0 = 300^\circ\text{K}$.

A transport correction was estimated by comparison of one dimensional radial and axial S_8 calculations with radial and axial diffusion calculations. (Flux weighted transport cross sections were used in the S_8 calculations.) The comparison led to a transport correction of +5.4 % for the Doppler coefficient.

A heterogeneity correction of +6% for core I-D and +5 % for core II-A for the Doppler coefficient A_D was derived from radial diffusion theory Doppler calculations for core I-D with

- a) heterogeneity corrected ZERA cross sections for the actual cell geometry, and
- b) ZERA cross sections with the cell dimensions reduced by a factor 10^3 ("quasi homogeneous" ZERA cross sections).

6.7 Comparison of Calculated with Experimental Results

Table VI summarizes the calculated results for the Doppler temperature coefficient A_D for core I-D and core 2-A for the MOXTOT set.

Table VI: Results of Nuclear Doppler Temperature Coefficient Calculations

Calculational Step	A_D	
	I-D	2-A
2 Dim. Diffusion, Perturbation Calculation, Including REMO Correction, $T_0 = 300 \text{ }^\circ\text{K}$.0083	.0062
Correction for Extrapolation to $T_0 = 1000 \text{ }^\circ\text{K}$	-.0008	-.0006
Heterogeneity Correction	+.0005	+.0003
Transport Correction	+.0004	+.0004 ^{*)}
Corrected Result	.0084	.0063

*) Assumed to be the same as calculated for I-D

The extrapolation to $1000 \text{ }^\circ\text{K}$ was performed, because this temperature is more representative for the experimental conditions in most of the SEFOR Doppler experiments.

The corrected results should be compared with the experimental results for A_D described in sections 3 and 4, which are listed in Table VII together with GE evaluation results / 6 /.

Table VII: Doppler Temperature Coefficient Evaluations
from Static and Transient Experiments

	Core I		Core II	
	GfK	GE	GfK	GE
Static Power Experiments	.0073	.0079	.0058	.0060
Transient Experiments	.0084	.0081	.0058	.0060
Average	.0079	.0080	.0058	.0060
Uncertainty of Evaluation	+.0012		+.0009	

It can be seen that calculated and evaluated Doppler temperature coefficients agree within the range of uncertainty of the evaluated numbers for both cores. A slight systematical overestimation (5 to 10 %) of A_D by MOXTOT calculations can be recognized. It can be expected from Table V that the overestimation would be reduced to the range 0 to 5 % in the case of the KfK INR set.

The calculated results as shown in Table VI do not contain the "non-NR" correction mentioned in section 6.2. This correction would increase the calculated coefficients by about 5 %.

The indicated overestimation of the Doppler temperature coefficient is in line with the overestimation of $1/\beta_{eff}$ and of fuel and boron reactivity worths (compare section 2). An increase of β_{eff} by about 5 % would generally improve the agreement between calculated and measured SEFOR parameters.

References for Section 6

- /1/ H. Huschke
Gruppenkonstanten für dampf- und natriumgekühlte schnelle Reaktoren in einer 26-Gruppendarstellung
KFK-770 (1968)
- /2/ E.A. Fischer
Interpretation von Dopplerproben-Messungen in schnellen kritischen Null-Energie-Anlagen
KFK-844 (1969)
- /3/ P.H. Kier, A.A. Robba
RABBLE, A Program for Computation of Resonance Absorption in Multiregion Reactor Cells
ANL-7326 (1967)
- /4/ H. Bogensberger, E.A. Fischer, A.M. Raberain, D. Wintzer
Dopplerrechnungen für schnelle Reaktoren - Standardverfahren und notwendige Korrekturen
Reaktortagung Hamburg (1972)
- /5/ O'Dell
Calculation of the Isothermal Doppler Coefficient for SEFOR
(Personal communication)
- /6/ L. Caldarola et al.
SEFOR Experimental Results and Application to LMFBR's
Proc. of the Int. Conf. on Engineering of Fast Reactors, Karlsruhe, Oct. 9 - 13, 1972

7. Summary and Conclusions

The analysis of the SEFOR zero power experiments leads to ratios between calculated and experimental results, which mostly are consistent with experience obtained by the analysis of more simple Plutonium fuelled configurations in zero power assemblies with the cross section sets MOXTOT and KFKINR. Exceptions with more pronounced differences between calculation and experiments are boron rod reactivity worths and fission rate distributions in Core I.

Nevertheless, the conclusion is permitted that there are no major errors in data and calculational procedures.

Doppler temperature coefficients derived from static power experiments and from transient experiments are in good agreement with GE evaluations, although different approximations have been used for the evaluation. Ratios between nuclear Doppler coefficient calculations and experimental numbers are in the range between 1.0 and 1.1 (for the KFKINR set and the MOXTOT set).

The transfer of experience obtained by SEFOR Doppler effect analysis to predictions for other LMFBR's requires the use of data and calculational procedures as described in this report, if the predictions should be based on the MOXTOT set or on the KFKINR set. It is suggested to use the Doppler temperature coefficient as calculated, with the only modification that the calculated effective fraction of delayed neutrons should be multiplied by 1.05. In the case of SEFOR, this procedure would reduce the difference to experimental Doppler coefficient data to insignificant amounts for both cross section sets.

Error estimates as described in /1/ indicate that this procedure of extrapolation to other LMFBR's would limit the uncertainty of the predicted Doppler power coefficient and of the Doppler energy coefficient to $\pm 25\%$ with a confidence level of about 90%.

A consistent transfer of the SEFOR analysis results for Doppler effect predictions in transient situations requires a correction of the calculated average decay constant of delayed neutrons and the inclusion of non-adiabatic effects in temperature calculations.

Reference for Section 7

- /1/ W.J. Oosterkamp, D. Wintzer
Übertragbarkeit der SEFOR-Dopplerergebnisse auf den SNR
KFK-1272/4 (1972), section 1216 SEFOR

A p p e n d i x A

Geometrical Models and Material Densities for
Neutrons Physics Calculations

Models for Two Dimensional Reactor Calculations

Figures 2.1 through 2.3 show the core loading pattern of Ass. 1-C, 1-D and 2-A. Corresponding two dimensional geometrical models of material distributions are shown in Fig. A1 and Fig. A2 for Ass. 1-C and 1-D.

Comments

Regions O, P and Q represent the central channel with slightly varying average steel concentrations along the channel axis. Regions A and B represent the regular core lattice with slightly lower BeO concentration and slightly higher steel concentration in B than in A. The core regions C and D differ from A and B because of the slightly (4%) lower Plutonium enrichment in the central 52 fuel rods. Regions E and F (in Ass. 1-D) differ from regions A and B because of the

FIG.A1 SEFOR - IC
GEOMETRICAL MODEL

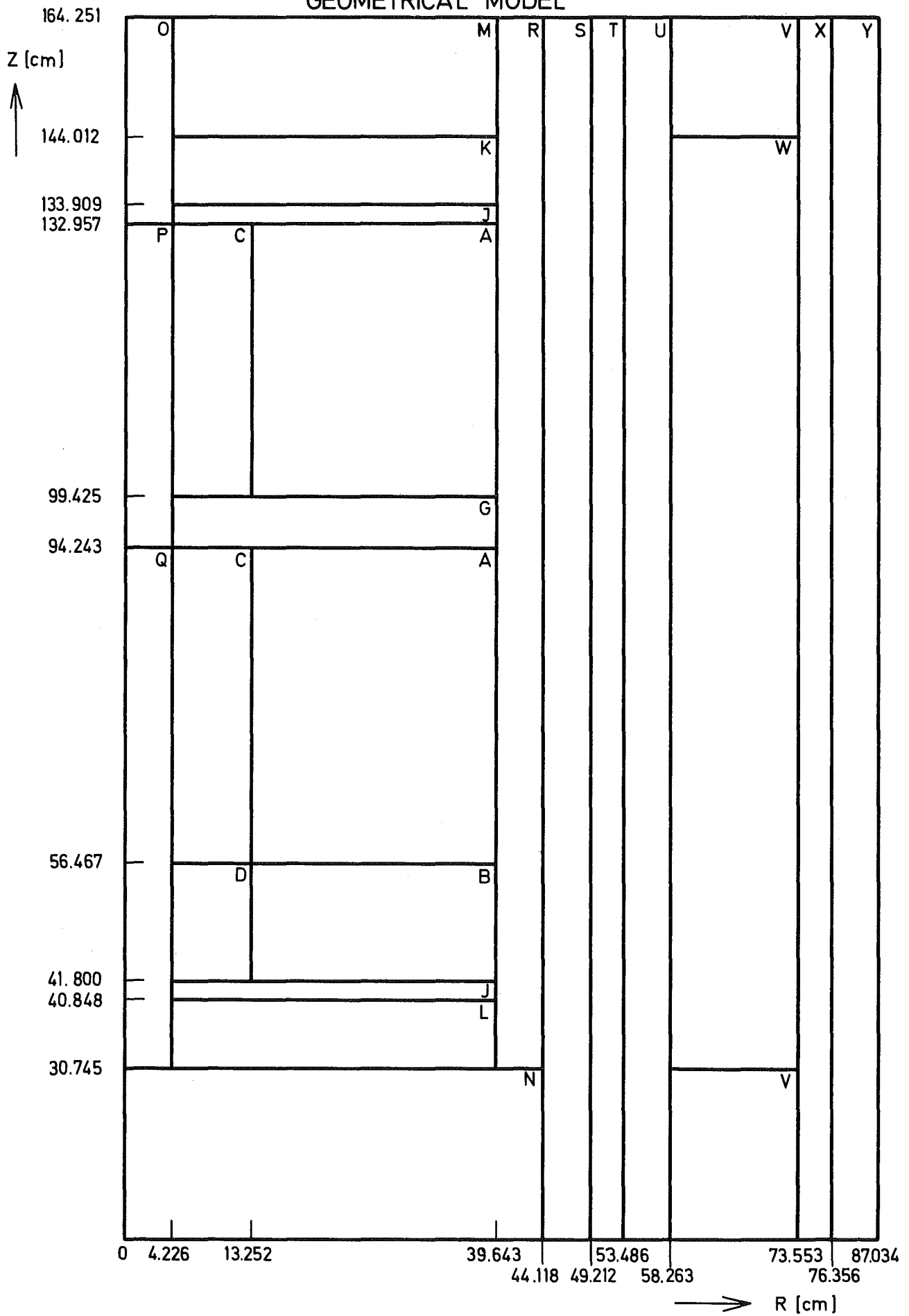
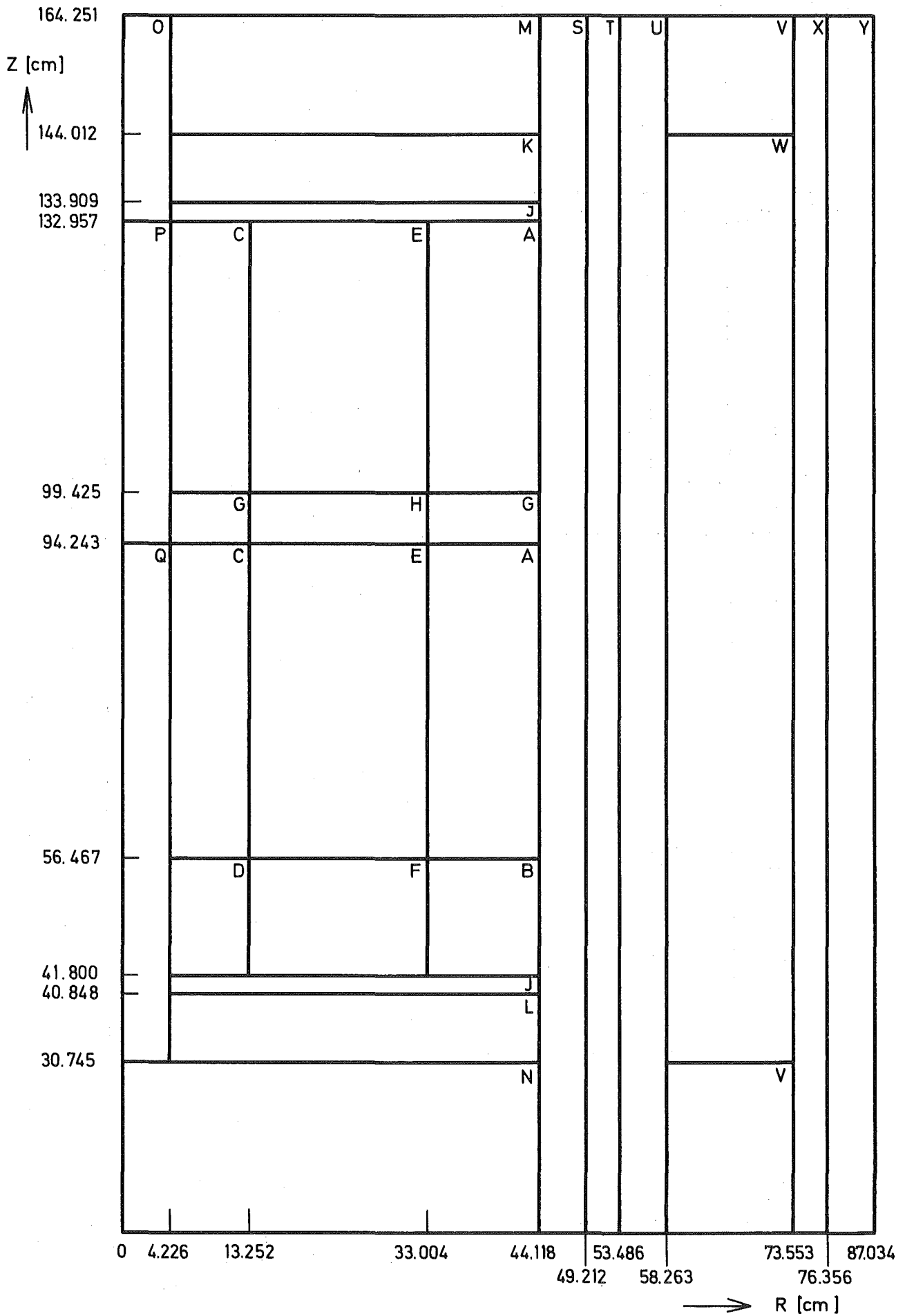


FIG. A2 SEFOR - ID



presence of the boron absorber rods in this region. The upper and lower parts of the core are separated by the gap regions G and H which essentially contain the springs of the expansion gaps and the UO_2 insulator pellets (compare Fig. A3). Regions I and J are for the upper and lower insulator pellets of the fuel rods. Nickel reflector regions are K, L (axial) and W (radial).

Region R represents that part of the core channel structure which was loaded with fuel elements in Ass. 1-C. The core edge plates, the shell around the core, torque rods and the corresponding volume of Na are homogenized in region S. Regions T and U represent the material of the, and around the, inner and outer vessel. Regions M, N, V, X and Y roughly describe various material structures beyond the axial and radial Ni reflectors.

The core composition of Ass. 2-A differs from Ass. 1-D because of the insertion of steel rods instead of the BeO rods (compare Fig. A4) to produce a harder neutron spectrum. In addition, Ass. 2-A contains 7 boron rods instead of 14 in Ass. 1-D.

Atom densities of the reactor regions are given in Table I. In addition to the regions shown in Figs. A1 and A2, Table I contains atom densities for additional regions above (M^+) and below (N^+ , N^{++}) regions M and N, respectively. The axial extensions of these regions are:

M^+	125.5 cm
N^+	40.4 cm
N^{++}	14.0 cm

Comparative criticality calculations yielded a reactivity increase of $\Delta k = .0014$ due to addition of these regions. Similar calculations showed a reactivity increase of $\Delta k = .0013$ for a transition from a more simple 4 region model for the radial material distribution beyond the core radius to the 6 region model (S, T, U, W, X, Y) as shown in Figs. A1 and A2.

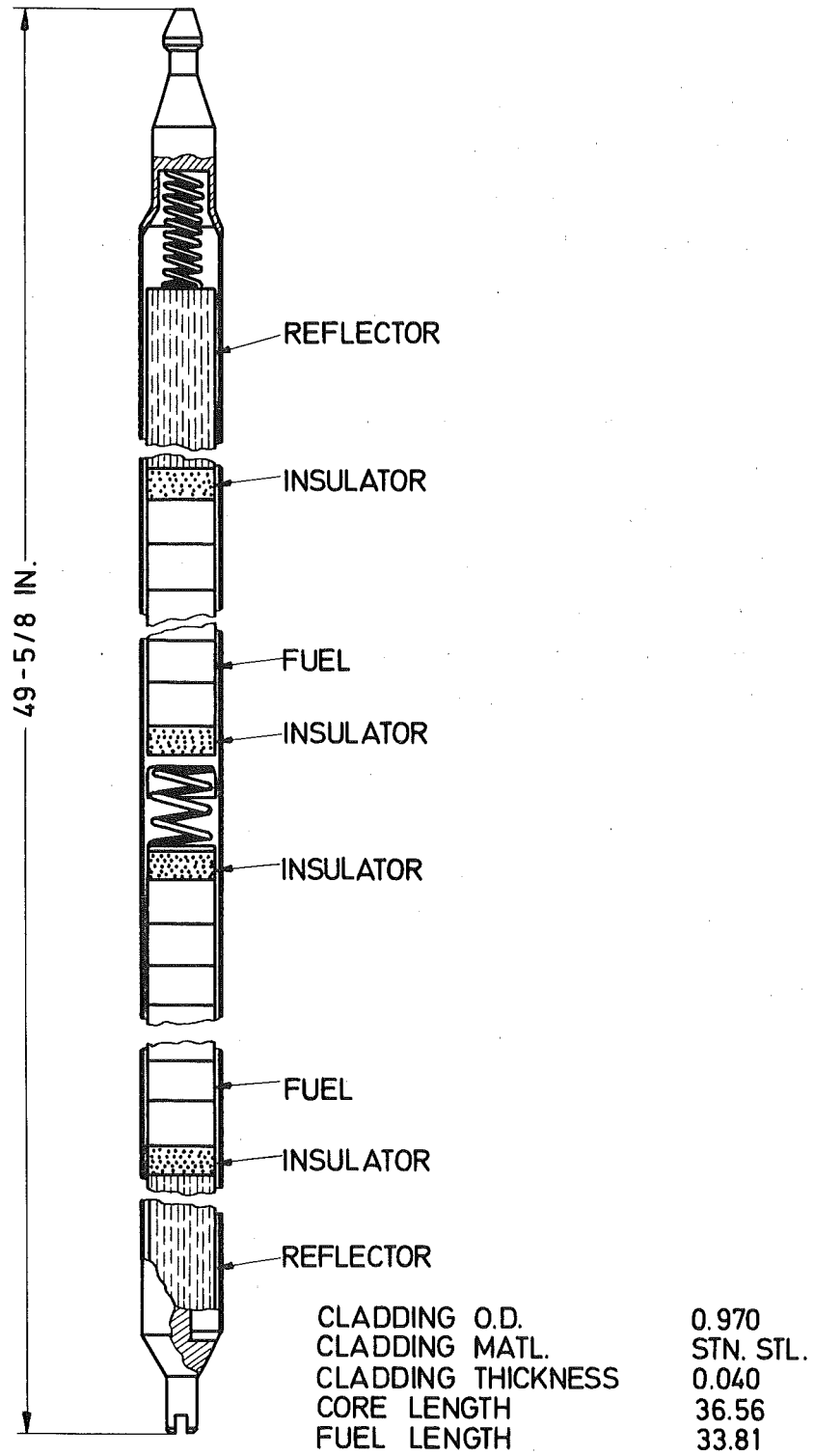


FIG. A3 SEFOR FUEL ROD

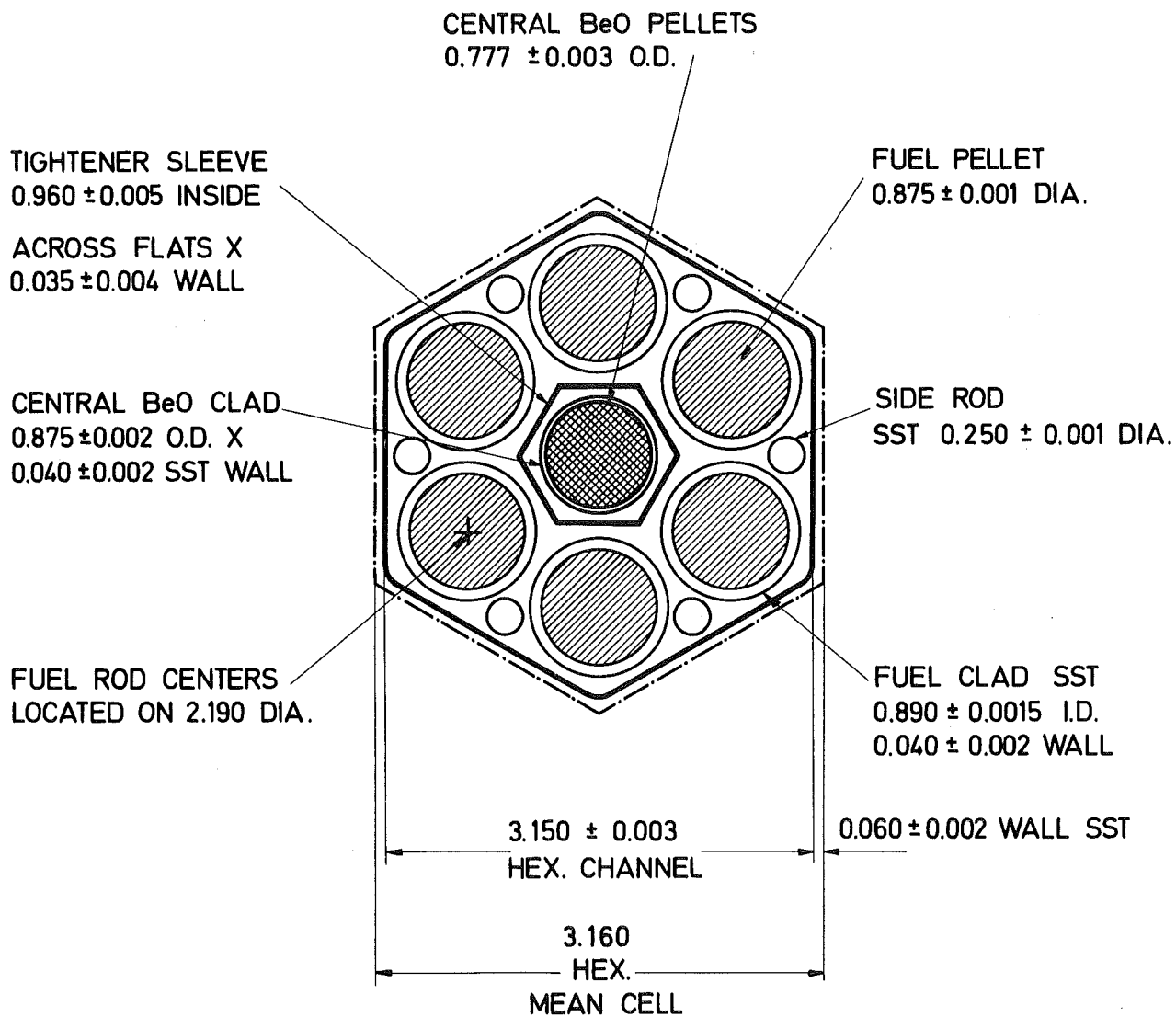


FIG. A4 SEFOR FUEL CHANNEL

Cell Models for Heterogeneity Calculations

Most of the Karlsruhe calculations for SEFOR are done with heterogeneity corrected microscopic cross sections for the core regions, which are computed by the cell code ZERA.

Two region models are used to describe the lattice cell (see Figs. A4 and A5). Cell region 1 represents a fuel rod (without clad) and cell region 2 represents Na, 1/6 of a BeO rod and the rest of the structural material. The cross sectional area of the unit cell is 1/6 of the cross sectional area of an element cell.

Table II contains the atom densities in the two cell regions for the cell models used. Homogenization of the atom densities within the cell yields the atom densities of the corresponding compositions of Table I.

The correspondence is:

<u>Cell No</u>	<u>Homog. Composition</u>
Z 1	A
Z 2	B
Z 3	C
Z 4	D
Z 7 (Z 5)	E
Z 8 (Z 6)	F

In Z 7 and Z 8, the lattice distortions due to the presence of some B_4C rods were approximated by slightly increasing (by a factor 22.05/21.05 - see Fig. A6) the unit cell area and by distributing the corresponding amount of B_4C in cell region 2.

For comparison calculations, another type of cell models (Z 5 and Z 6) is used for the homogeneous compositions E and F. They describe a boron rod (see Fig. A7) in the center of the cell (cell region 1), the rest of the usual rod cell in cell region 2 and homogenized core material without B_4C in a third cell region. The cross sectional area of Z 5 and Z 6 is 1/14 of the cross sectional area occupied by compositions E and F.

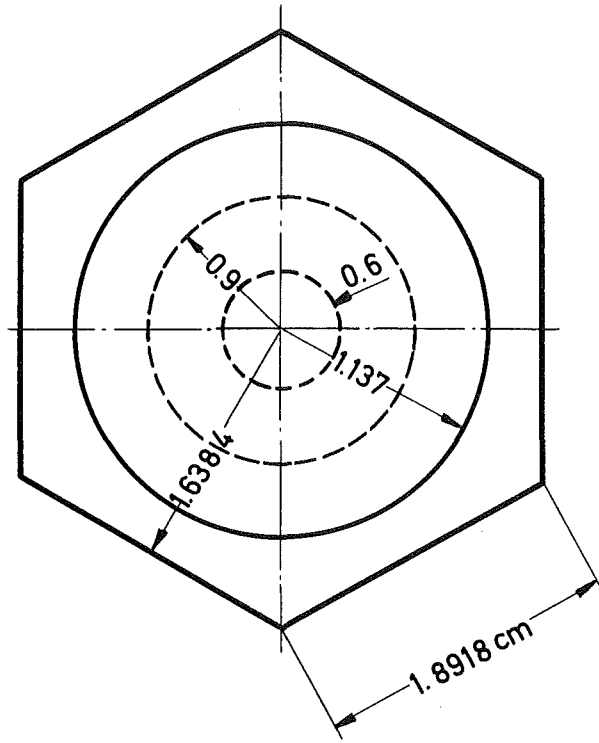


FIG. A5

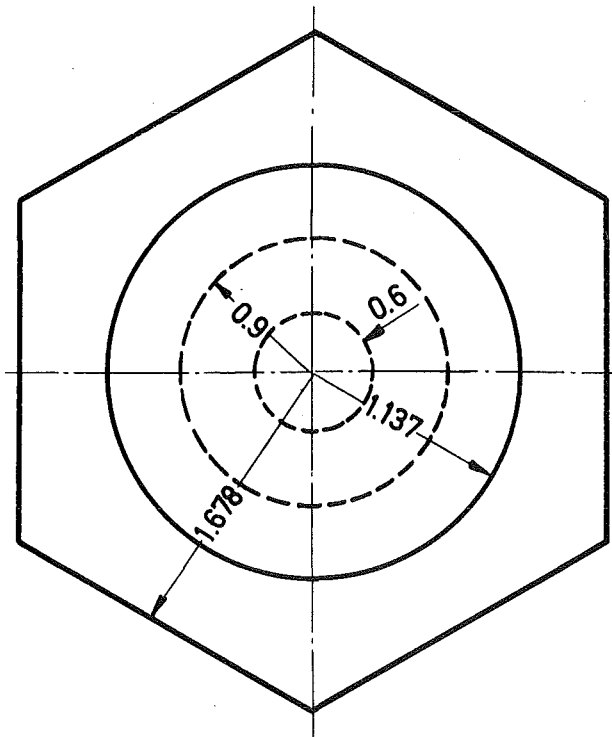


FIG. A6

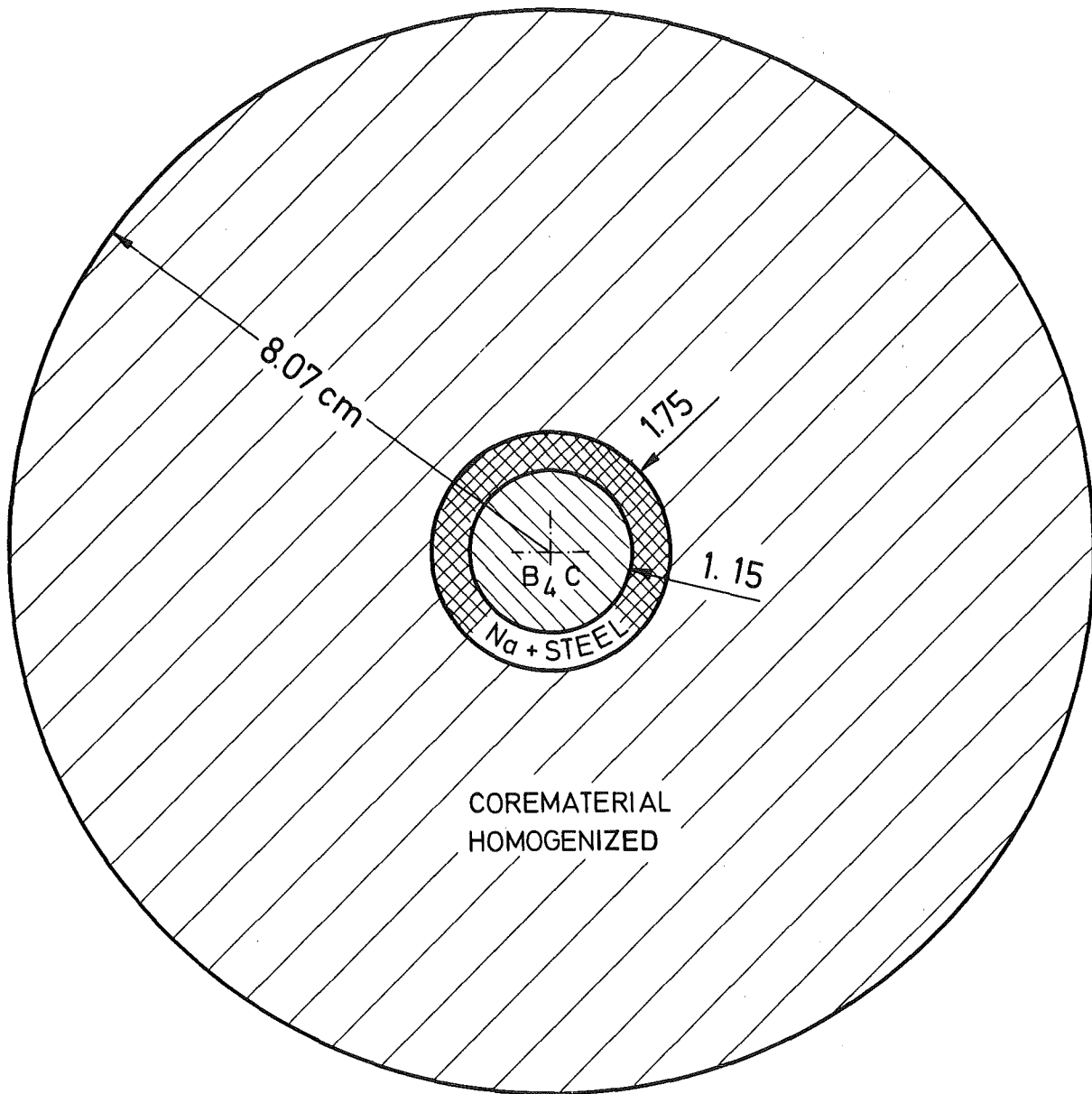


FIG. A7 CELL MODEL FOR BORON
ROD CELL CALCULATIONS

TABLE I

Atom Densities in SEFOR Compositions

	A	B	C	D	E	F	G	H
Be	3.7769-3	2.6840-3	3.7769-3	2.6840-3	3.7769-3	2.6840-3	3.7769-3	3.7769-3
B-10	-	-	-	-	1.4402-4	1.4402-4	-	1.4402-4
B-11	-	-	-	-	5.7968-4	5.7968-4	-	5.7968-4
C	-	-	-	-	1.8092-4	1.8092-4	-	1.8092-4
O	2.2146-2	2.1052-2	2.2146-2	2.1052-2	2.1313-2	2.0219-2	1.0742-2	1.0360-2
Al	-	-	-	-	-	-	-	-
Na	6.8099-3	6.8099-3	6.8099-3	6.8099-3	6.8099-3	6.8099-3	6.8099-3	6.8099-3
Cr	3.7929-3	3.9587-3	3.7929-3	3.9587-3	3.9322-3	4.0978-3	5.1147-3	5.1939-3
Fe	1.3368-2	1.3952-2	1.3368-2	1.3952-2	1.3846-2	1.4430-2	1.7330-2	1.7628-2
Ni	2.2297-3	2.3272-3	2.2297-3	2.3272-3	2.3011-3	2.3987-3	3.6265-3	3.6345-3
Mo	1.1915-4	1.2436-4	1.1915-4	1.2436-4	1.1915-4	1.2436-4	1.1915-4	1.1915-4
U-235	1.6154-5	1.6154-5	1.6303-5	1.6303-5	1.5421-5	1.5421-5	7.6230-6	7.2773-6
U-238	7.3328-3	7.3328-3	7.4005-3	7.4005-3	7.0002-3	7.0002-3	3.4578-3	3.3010-3
Pu-239	1.7215-3	1.7215-3	1.6595-3	1.6595-3	1.6434-3	1.6434-3	-	-
Pu-240	1.5506-4	1.5506-4	1.4948-4	1.4948-4	1.4803-4	1.4803-4	-	-

TABLE I (continued)

Atom Densities in SEFOR Compositions

	I	J	K	L	M	M ⁺	N	N ⁺	N ⁺⁺	O	P
Be	3.7705-3	2.6912-3	-	-	-	-	-	-	-	-	-
B-10	-	-	-	-	-	6.579-3	-	-	-	-	-
B-11	-	-	-	-	-	2.632-2	-	-	-	-	-
C	-	-	-	-	-	8.224-3	-	-	-	-	-
O	2.2748-2	2.1669-2	-	-	-	-	-	-	-	-	-
Al	-	-	-	-	-	-	-	-	-	-	-
Na	6.8099-3	6.8099-3	6.8759-3	6.9716-3	1.3526-2	9.83-3	1.081-2	2.40-2	3.43-3	1.6615-2	1.6615-2
Cr	3.7929-3	3.9587-3	3.9153-3	3.6070-3	5.9192-3	2.40-3	9.46 -3	-	1.51-2	3.1760-3	2.0624-3
Fe	1.3368-2	1.3952-2	1.3784-2	1.2732-2	1.8825-2	8.41-3	3.00 -2	-	5.20-2	1.0894-2	7.0745-3
Ni	2.2297-3	2.3272-3	4.2413-2	4.306-2	3.1419-3	1.20-3	5.30 -3	-	7.77-3	1.6285-3	1.0575-3
Mo	1.1915-4	1.2436-4	1.2909-4	1-1974-4	1.2872-4	5.48-5	-	-	-	-	-
U-235	2.0670-5	2.0670-5	-	-	-	-	-	-	-	-	-
U-238	9.4207-3	9.4207-3	-	-	-	-	-	-	-	-	-
Pu-239	-	-	-	-	-	-	-	-	-	-	-
Pu-240	-	-	-	-	-	-	-	-	-	-	-

TABLE I (continued)

Atom Densities in SEFOR Regions

	Q	R	S	T	U	V	W	X	Y
Be	-	-	-	-	-	-	-	-	-
B-10	-	-	-	-	-	-	-	-	6.63-3
B-11	-	-	-	-	-	-	-	-	2.72-2
C	-	-	-	-	-	-	-	-	8.45-3
O	-	-	-	-	-	-	-	-	-
Al	-	-	-	-	1.1791-2	-	2.1303-3	2.7290-2	-
Na	1.6615-2	2.0790-2	1.4943-2	1.4496-2	-	-	-	-	-
Cr	5.3564-3	2.2978-3	6.4971-3	4.1208-3	2.7620-3	2.659-3	5.9730-4	1.0186-3	1.86-3
Fe	1.8373-2	7.8820-3	2.0600-2	1.4135-2	9.4740-3	9.093-3	2.0489-3	3.4939-3	5.73-3
Ni	2.7465-3	1.1782-3	5.4525-3	2.1129-3	1.4160-3	1.364-3	7.3936-2	5.2226-4	1.01-3
Mo	-	-	-	-	-	-	-	-	-
U-235	-	-	-	-	-	-	-	-	-
U-238	-	-	-	-	-	-	-	-	-
Pu-239	-	-	-	-	-	-	-	-	-
Pu-240	-	-	-	-	-	-	-	-	-

TABLE II

Cell Compositions for Heterogeneity Calculations

	CELL Z1		CELL Z2		CELL Z3		CELL Z4	
	Region 1	Region 2	Region 1	Region 2	Region 1	Zone 2	Zone 1	Zone 2
Be	-	6.501-3	-	4.620-3	-	6.501-3	-	4.620-3
O	4.383-2	6.501-3	4.383-2	4.620-2	4.383-2	6.501-3	4.383-2	4.620-3
Na	-	1.172-2	-	1.172-2	-	1.172-2	-	1.172-2
Cr	-	6.529-3	-	6.814-3	-	6.529-3	-	6.814-3
Fe	-	2.301-2	-	2.402-2	-	2.301-2	-	2.402-2
Ni	-	3.838-3	-	4.006-3	-	3.838-3	-	4.006-3
Mo	-	2.051-4	-	2.141-4	-	2.051-4	-	2.141-4
U-235	3.855-5	-	3.855-5	-	3.890-5	-	3.890-5	-
U-238	1.750-2	-	1.750-2	-	1.766-2	-	1.766-2	-
Pu-239	4.108-3	-	4.108-3	-	3.960-3	-	3.960-3	-
Pu-240	3.700-4	-	3.700-4	-	3.567-4	-	3.567-4	-
						-		-

Cell Geometry : I (see Fig. 7A)

TABLE II (continued)

CELL COMPOSITIONS FOR HETEROGENEITY CALCULATIONS

CELL Z5			
	Region 1	Region 2	Region 3
Be	-	6.501-3	3.7769-3
B-10	7.5775-3	-	-
B-11	3.0500-2	-	-
C	9.5192-3	-	-
O	-	6.501-3	2.2146-2
Na	-	1.172-2	6.8099-3
Cr	7.3262-3	6.529-3	3.7929-3
Fe	2.5130-2	2.301-2	1.3368-2
Ni	3.7564-3	3.838-3	2.2297-3
Mo	-	2.051-4	1.1915-4
U-235	-	-	1.6154-5
U-238	-	-	7.3328-3
Pu-239	-	-	1.7215-3
Pu-240	-	-	1.5506-4

CELL Z6			
	Region 1	Region 2	Region 3
Be	-	4.620-3	2.6840-3
B-10	7.5775-3	-	-
B-11	3.0500-2	-	-
C	9.5192-3	-	-
O	-	4.620-3	2.1052-2
Na	-	1.172-2	6.8099-3
Cr	7.3262-3	6.814-3	3.9587-3
Fe	2.5130-2	2.402-2	1.3952-2
Ni	3.7564-3	4.006-3	2.3272-3
Mo	-	2.141-4	1.2436-4
U-235	-	-	1.6154-5
U-238	-	-	7.3328-3
Pu-239	-	-	1.7215-3
Pu-240	-	-	1.5506-4

CELL GEOMETRY: 3 (see Fig. 7C)

TABLE II (continued)

CELL COMPOSITIONS FOR HETEROGENEITY CALCULATIONS

	Cell Z 7		Cell Z 8	
	Region 1	Region 2	Region 1	Region 2
Be	-	6.2953-3	-	4.4737-3
B-10	-	2.4005-4	-	2.4005-4
B-11	-	9.6621-4	-	9.6621-4
C	-	3.0156-4	-	3.0156-4
O	4.383-2	6.299-3	4.383-2	4.475-3
Na	-	1.1351-2	-	1.1351-2
Cr	-	6.554-3	-	6.8302-3
Fe	-	2.3079-2	-	2.4052-2
Ni	-	3.8355-3	-	3.9932-3
Mo	-	1.986-4	-	2.0728-4
U-235	3.855-5	-	3.855-5	-
U-238	1.750-2	-	1.750-2	-
Pu-239	4.108-3	-	4.108-3	-
P-240	3.700-4	-	3.700-4	-

CELL GEOMETRY: 2 (see Fig. 7 B)

A p p e n d i x B

Supplementary Studies for B₄C Rods in SEFOR 1-D

Flux Depressions in and Around Boron Rods

ZERA cell calculations for a representative boron rod containing core cell were performed for evaluation of neutron flux and reaction rate depressions in and around the SEFOR B₄C rods. Cell geometry and material densities are shown in Fig. A7 and Table II (cell Z 5) of Appendix A. The ratio of core material over B₄C in the cell corresponds to the average ratio in core region E of Ass. 1-D (see Fig. A2). Figures B1 and B2 show radial flux distributions for some neutron energy groups. Flux depressions in the vicinity of the B₄C rods are substantial at high energies (because of lacking neutron sources) and at low energies (because of high B-10 absorption cross sections at low energies). About 2/3 of the boron absorption occurs in the energy range between 20 keV and 200 keV, where the flux depression is not substantial. The resulting reduction of the B₄C absorption compared to a corresponding homogeneous case is 6 per cent.

Effects of Asymmetrical B_4C Loadings in the Core

It was pointed out in section 2.3 that the B_4C rod loading in Ass. 1-D was not quite symmetrical, and it was suspected that this fact contributed to the overestimation of the reactivity worths of B_4C rods and fuel rods in this assembly by the calculations. An attempt was made to estimate the resulting asymmetry effect by r- geometry diffusion calculations. Fig. B3 shows the model of material distribution for this study. The boron containing core region extends from a radius of 13.252 cm. The model represents 8 boron rods in the right half section of the core (see Fig. B3) and 6 boron rods in the left half section.

The calculated angular distribution of the neutron flux in energy groups 1 and 4 is shown in Fig. B4 for a radial position of 33 cm (compare Fig. B3). Calculated angular distributions of fission rates are shown in Figs. B5 through B7 for ^{238}U , ^{239}Pu , and ^{235}U . The square of the ^{239}Pu fission rate distribution is a rough estimate of the reactivity worth distribution and indicates a reactivity worth difference in the order of 8 per cent between the left hand side and the right hand side (Fig. B3) of the core at $r = 33$ cm.

The material distribution model for these calculations somewhat overestimates the actual asymmetry of the B_4C loading in Ass. 1-D, and a more exact description of the boron distribution would probably lead to a reactivity difference of about 6% instead of 8%. It was mentioned in section 2.3 that this is the order of magnitude of the asymmetry effect on reactivity worth measurements, which was indicated by some experimental numbers. The effect is probably one of the reasons for the more pronounced overestimation of material reactivity worths in Ass. 1-D than in Ass. 2-A (the latter had a fairly symmetrical boron loading).

FIG. B1 FLUX DISTRIBUTION AROUND B₄C RODS

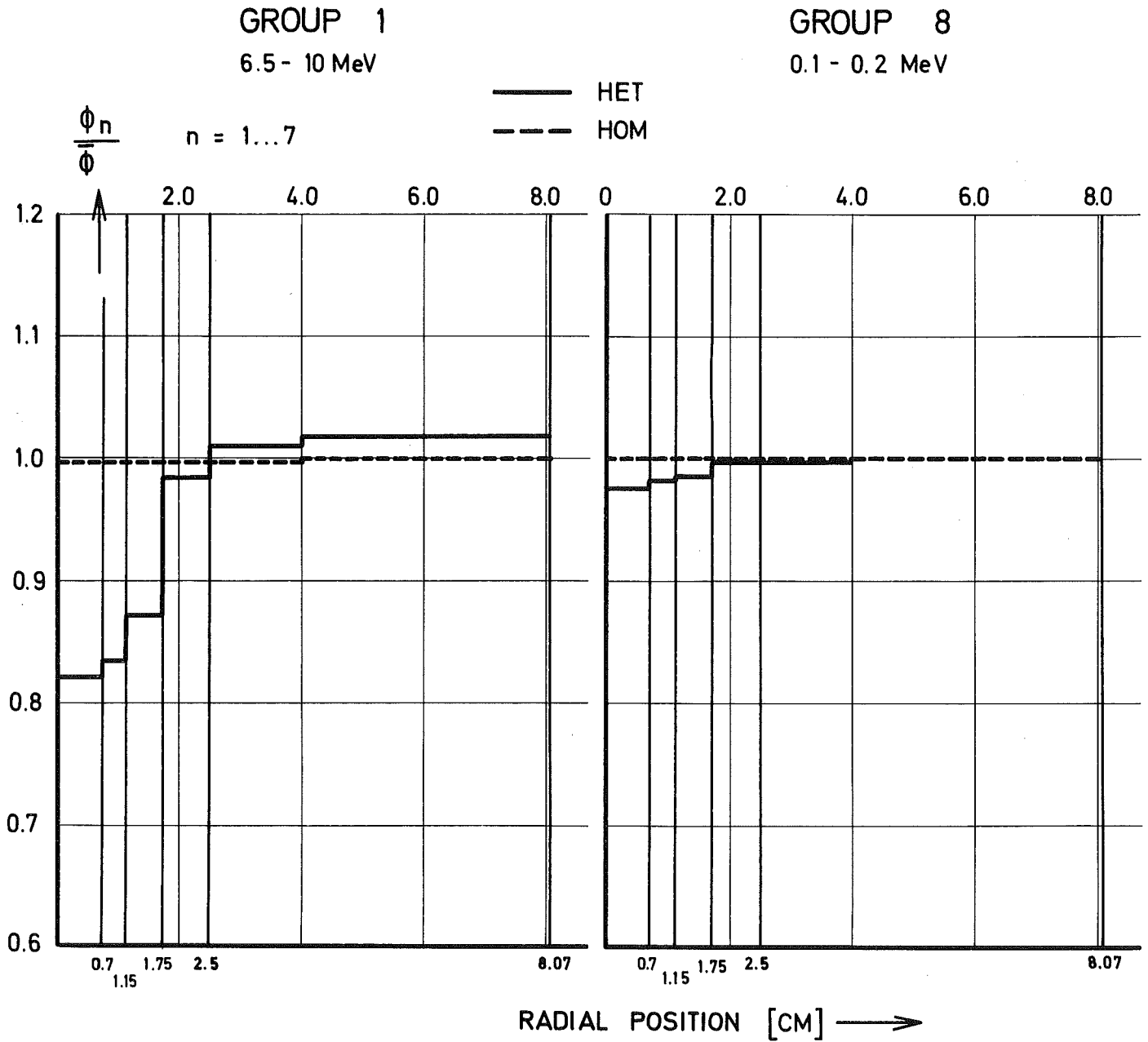
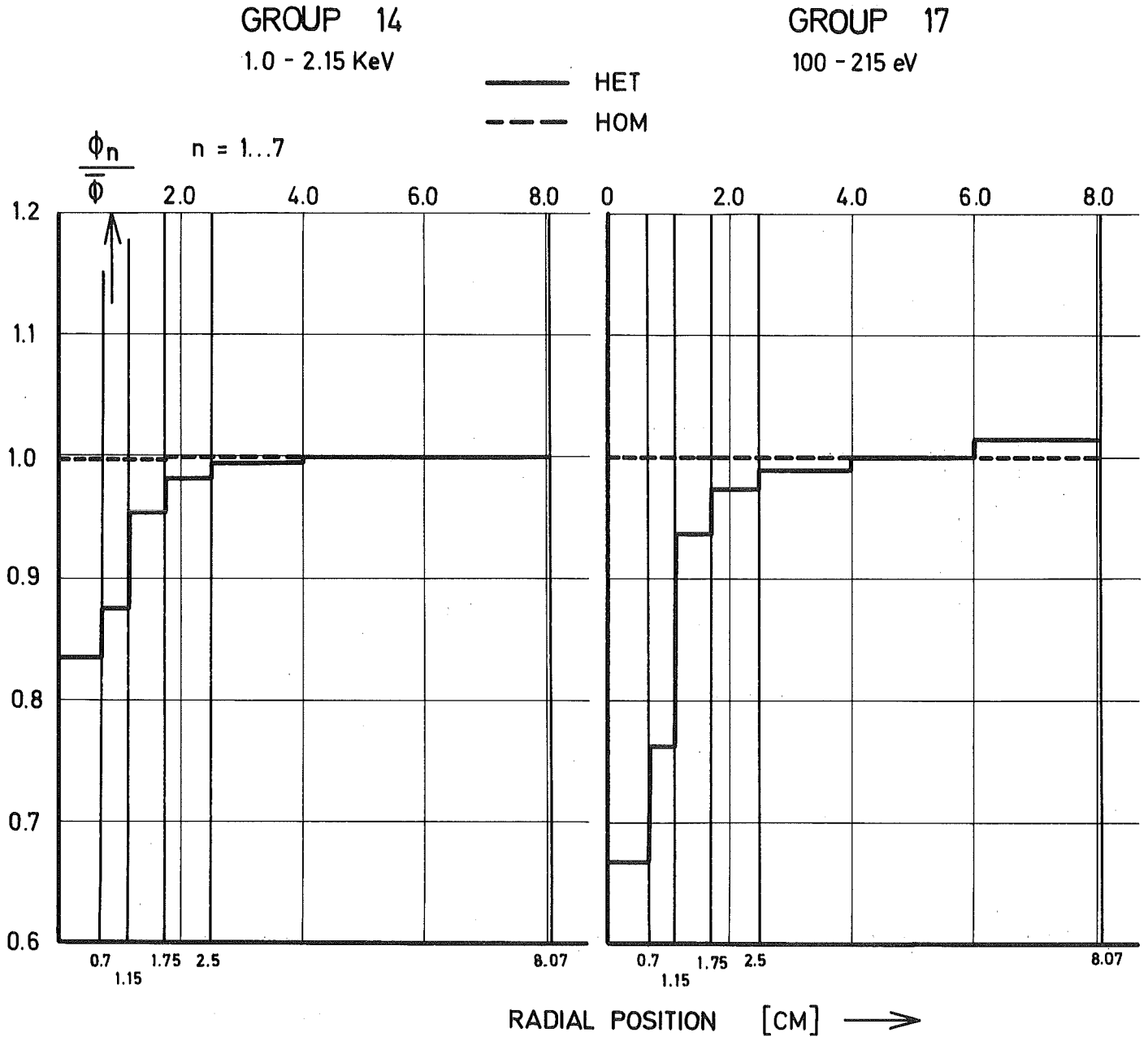


FIG.B2 FLUX DISTRIBUTION AROUND B₄C RODS



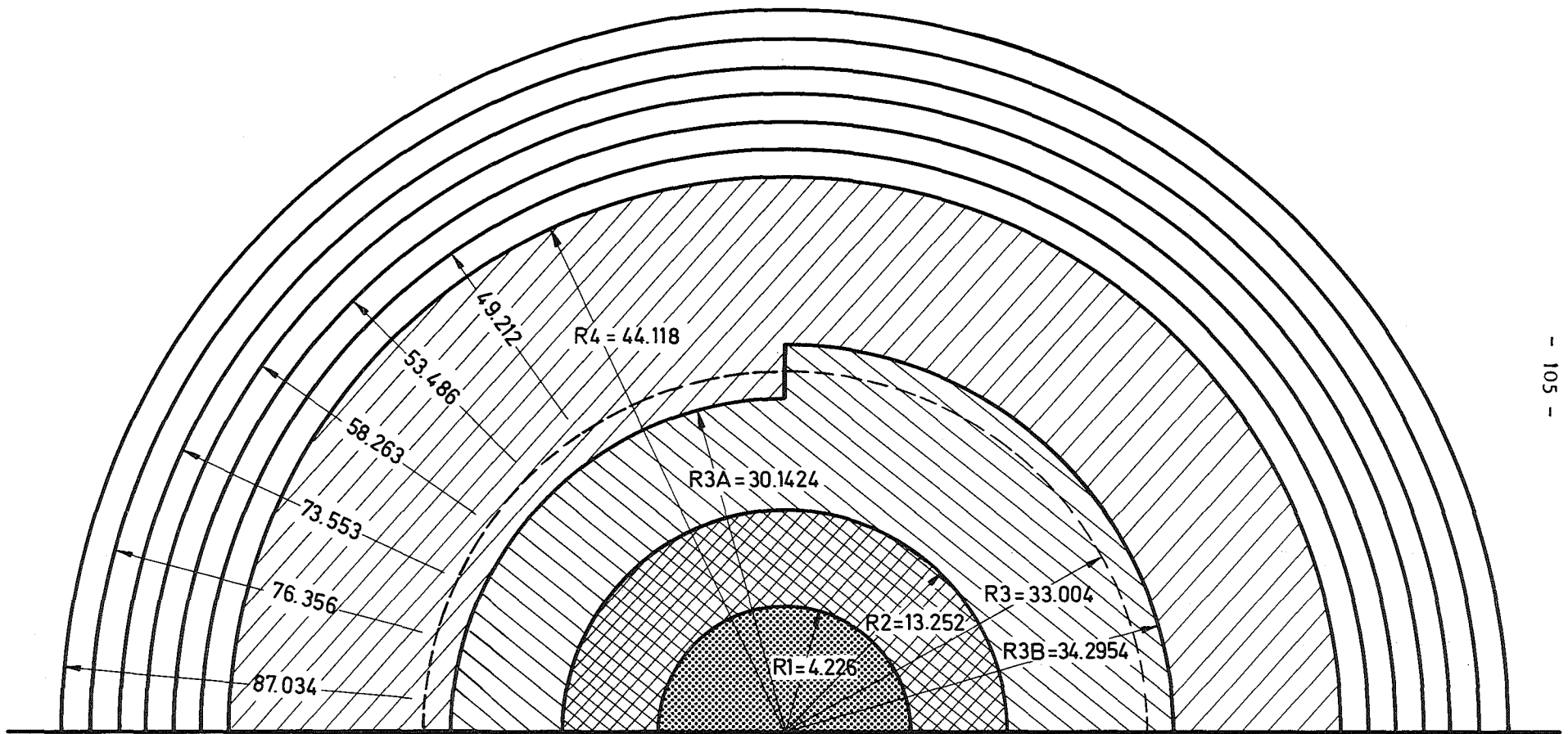


FIG.B3 Core 1D R θ - Geometrie

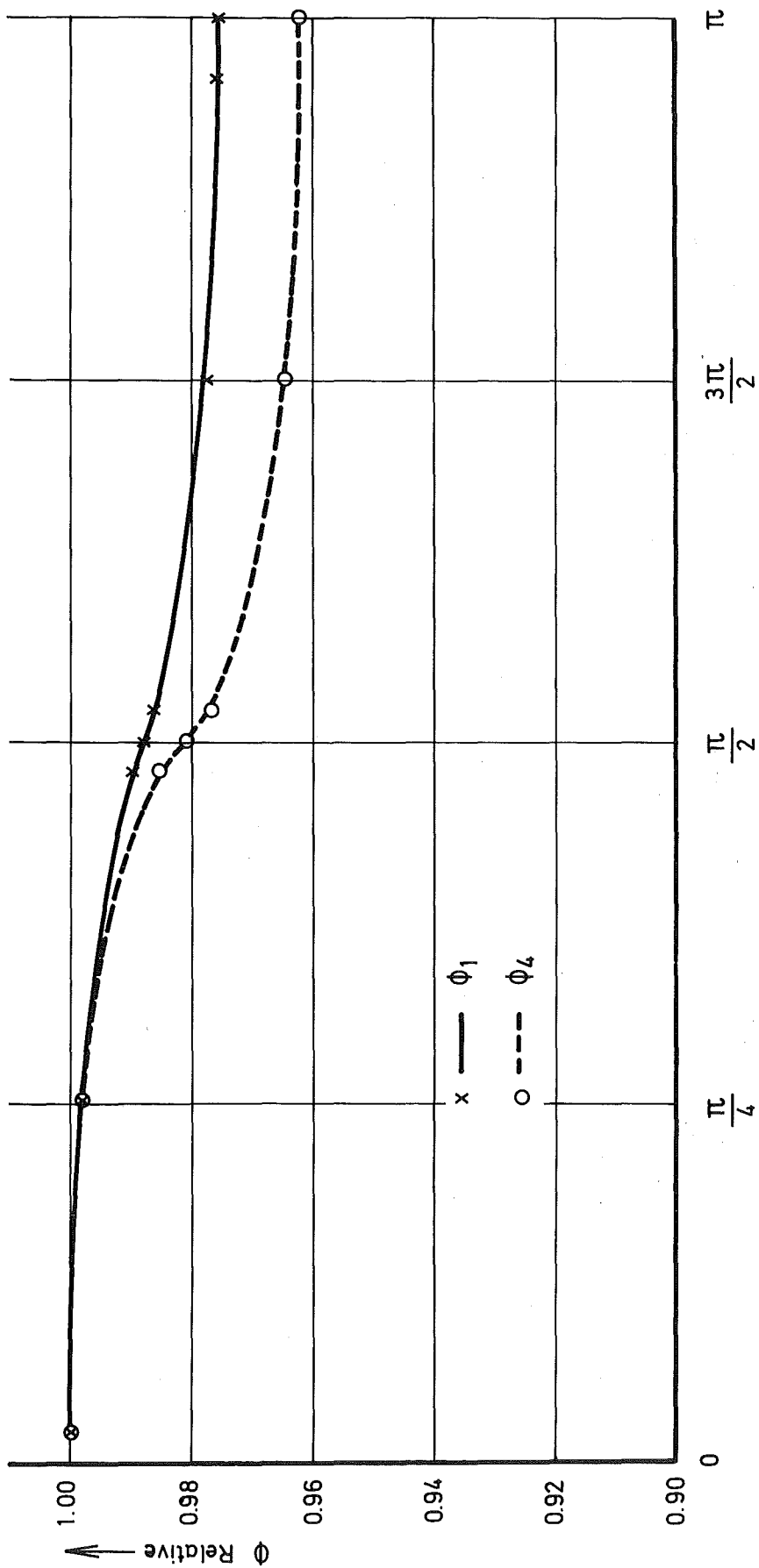


Fig. B4 Relative Flux Distribution

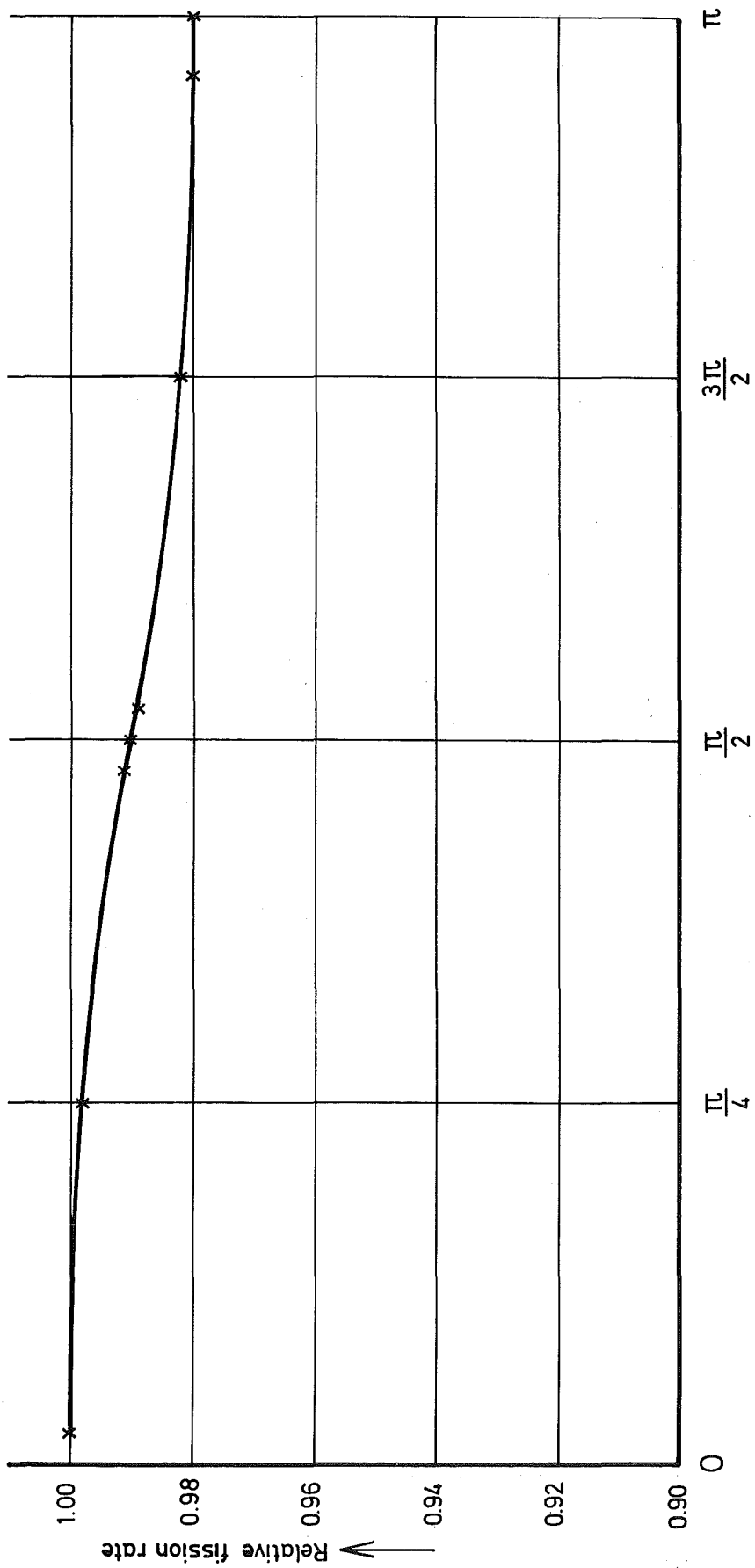


Fig. B5 Fission Rate Traverse U238

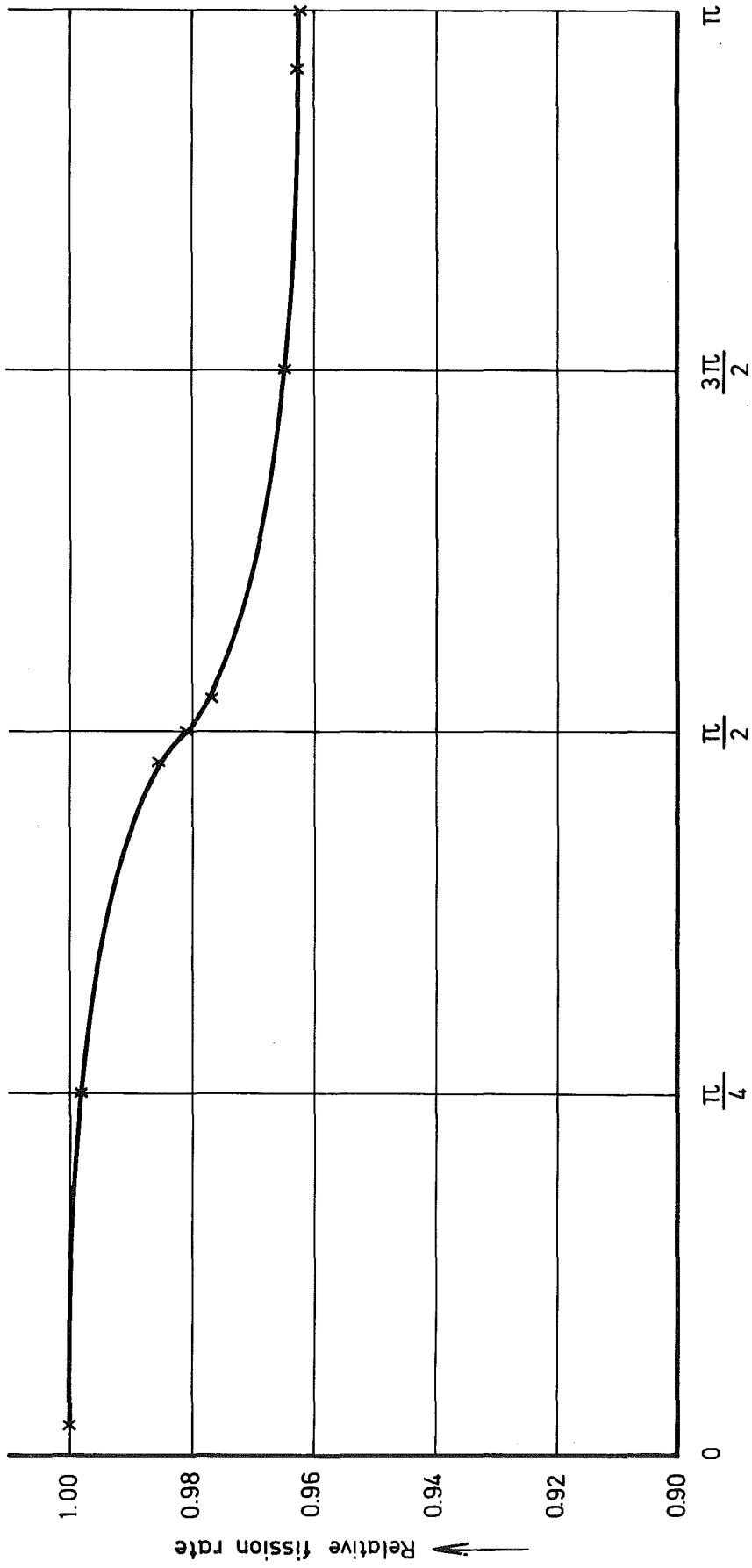


Fig. B6 Fission Rate Traverse Pu 239

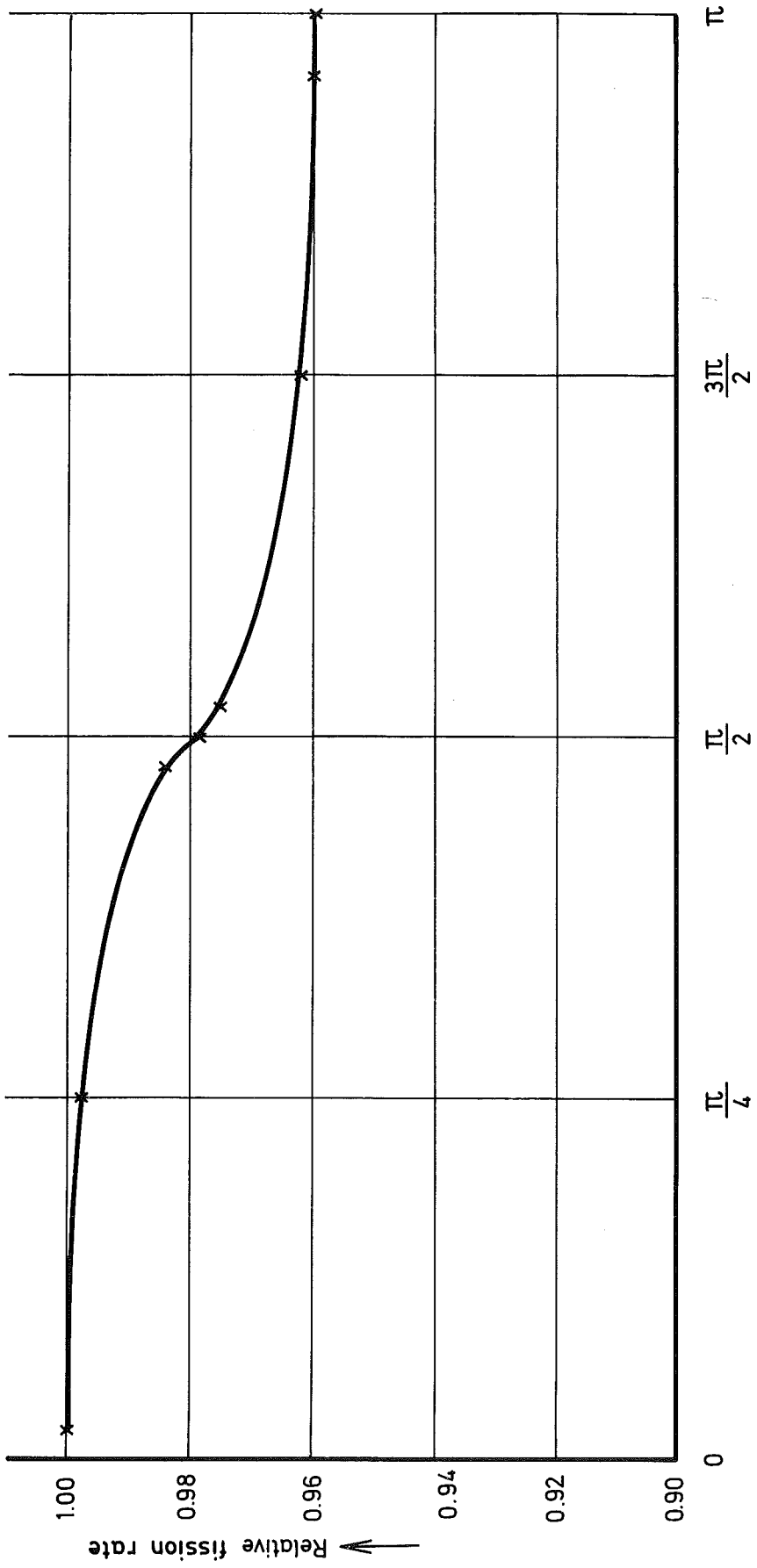


Fig. B7 Fission Rate Traverse U 235